Journal of the American Heart Association

ORIGINAL RESEARCH

Spontaneous Degenerative Aortic Valve Disease in New Zealand Obese Mice

Christiane Ott (iD), PhD; Kathleen Pappritz, PhD; Niklas Hegemann, MSc; Cathleen John (iD), PhD; Sarah Jeuthe, PhD; Cameron S. McAlpine, PhD; Yoshiko Iwamoto, BS; Jonathan H. Lauryn, MD; Jan Klages, MD; Robert Klopfleisch, MD; Sophie Van Linthout, PhD; Fil Swirski (iD), PhD; Matthias Nahrendorf (iD), MD; Ulrich Kintscher (iD), MD; Tilman Grune (iD), PhD; Wolfgang M. Kuebler, MD;* Jana Grune (iD), PhD*

BACKGROUND: Degenerative aortic valve (AoV) disease and resulting aortic stenosis are major clinical health problems. Murine models of valve disease are rare, resulting in a translational knowledge gap on underlying mechanisms, functional consequences, and potential therapies. Naïve New Zealand obese (NZO) mice were recently found to have a dramatic decline of left ventricular (LV) function at early age. Therefore, we aimed to identify the underlying cause of reduced LV function in NZO mice.

METHODS AND RESULTS: Cardiac function and pulmonary hemodynamics of NZO and age-matched C57BL/6J mice were monitored by serial echocardiographic examinations. AoVs in NZO mice demonstrated extensive thickening, asymmetric aortic leaflet formation, and cartilaginous transformation of the valvular stroma. Doppler echocardiography of the aorta revealed increased peak velocity profiles, holodiastolic flow reversal, and dilatation of the ascending aorta, consistent with aortic stenosis and regurgitation. Compensated LV hypertrophy deteriorated to decompensated LV failure and remodeling, as indicated by increased LV mass, interstitial fibrosis, and inflammatory cell infiltration. Elevated LV pressures in NZO mice were associated with lung congestion and *cor pulmonale*, evident as right ventricular dilatation, decreased right ventricular function, and increased mean right ventricular systolic pressure, indicative for the development of pulmonary hypertension and ultimately right ventricular failure.

CONCLUSIONS: NZO mice demonstrate as a novel murine model to spontaneously develop degenerative AoV disease, aortic stenosis, and the associated end organ damages of both ventricles and the lung. Closely mimicking the clinical scenario of degenerative AoV disease, the model may facilitate a better mechanistic understanding and testing of novel treatment strategies in degenerative AoV disease.

Key Words: aortic stenosis ■ *cor pulmonale* ■ degenerative aortic valve disease ■ global heart failure ■ pulmonary hypertension

Among cardiovascular diseases, aortic stenosis (AS) is the most common primary valve disease, with a growing prevalence in the aging population.[1] In patients aged ≥75 years, the prevalence of AS is 2.8%, making AS a main cause of cardiovascular morbidity and mortality, independent of the underlying cause.[2–4] Apart from congenital cardiac malformations, like bicuspid aortic valves (AoVs), gradually progressive degenerative AoV disease (DAVD) is the most frequent cause for AS in the Western world.[5,6] Morphological hallmarks of degenerative AoVs include matrix remodeling, endothelial dysfunction, lipid deposition, inflammatory cell infiltration, and finally severe calcification of the valvular stroma, causing a pathophysiologic continuum ranging from mild valve thickening without relevant hemodynamic changes to impaired leaflet motion.[7] The latter results in a progressive increase in left ventricular (LV) afterload that is initially matched by LV hypertrophy to maintain cardiac output. However, as the disease advances chronically, elevated LV

JAHA is available at: www.ahajournals.org/journal/jaha

CLINICAL PERSPECTIVE

What Is New?

- Herein, we report male New Zealand obese mice as a novel model of spontaneous degenerative aortic valve disease, which causes aortic stenosis and a complex cardiopulmonary phenotype at early age.
- We found dysregulated matricellular protein composition and impaired extracellular matrix maturation as a core mechanism for the development of degenerative aortic valve disease in New Zealand obese mice.

What Are the Clinical Implications?

- The cardiopulmonary phenotype of New Zealand obese mice replicates the characteristic phenotype of clinical aortic stenosis, attesting to the high translatability of this commercially available model for studies of spontaneous degenerative aortic valve disease, aortic stenosis, and the associated cardiopulmonary end-organ damage.
- This novel research tool paves the way for a detailed investigation of molecular and morphological mechanisms underlying degenerative aortic valve disease and may serve as a platform for the development of novel treatment strategies.

Nonstandard Abbreviations and Acronyms

AoV	aortic valve
AR	aortic regurgitation
AS	aortic stenosis
DAVD	degenerative aortic valve disease
NZO	New Zealand obese
PH	pulmonary hypertension

end-diastolic pressure ultimately results in LV dilatation and failure.[8] Subsequent secondary pulmonary hypertension (PH) and ultimately right ventricular (RV) failure present frequent and serious complications with poor clinical outcome in patients with severe AS.[9,10] This fatal progression of DAVD is orchestrated by multiple risk factors, including male sex, age, obesity, and dyslipidemia, further accelerating the disease process.[11–14]

Although this pathophysiological sequence is well characterized, the underlying mechanisms of DAVD remain poorly understood, at least in part because of the lack of appropriate preclinical animal models. Despite the high clinical prevalence of AS, murine models of valve diseases are rare, often based on complex intervention strategies, and commonly lack significant hemodynamic stenosis that is critical for the development of the clinical phenotype.[15–18] Today, surgical intervention remains the only option to treat AS through valve replacement or transcatheter AoV implantation, highlighting the unmet clinical need for developing drug target-based therapeutic strategies for the treatment or prevention of DAVD and AS.[19]

The New Zealand obese (NZO) mouse is an established polygenic model for metabolic syndrome and type 2 diabetes.[20] When fed a high-fat diet, these mice become morbidly obese, with associated hypertension, hyperinsulinemia, and hypercholesterolemia.[21] Recently, however, we identified a dramatic decline in LV function and markedly enlarged LV volumes in *naïve* male NZO mice on normal chow at 22 weeks of age, suggesting a congenital and progressive heart disease of unknown cause in this strain.[22] By state-of-the-art echocardiographic imaging and histological analyses, we aimed to identify the pathophysiologic mechanism underlying this phenotype. Hereinafter, we report NZO mice as a novel mouse model with spontaneous development of DAVD and AS, resulting in a complex cardiopulmonary phenotype of LV failure, lung congestion, PH, and ultimately RV failure, that mimics the clinical presentation of patients with AS. Our discovery of a murine model with spontaneous AS development holds promise as it represents a novel preclinical tool to investigate mechanisms of degenerative valve diseases and their pathophysiological effects on LV and RV structure and function, and to test for potential therapeutic interventions.

METHODS

The data that support the findings of this study are available from the corresponding author on reasonable request. All animal procedures were performed in accordance with the *Guide for the Care and Use of Laboratory Animals* (Institute of Laboratory Animal Resources, 7th edition, 1996) and the European legislation for animal welfare (Directive 2010/63/EU). All procedures were approved by the local authorities (G0239/16, 2347-5-2017) and in accordance with institutional guidelines. Detailed description of methods can be found in Data S1.

Animals

All mice were fed a normal rodent chow (Ssniff Spezialdiäten GmbH, Soest, Germany) and had identical housing conditions. Cardiovascular function was monitored by serial echocardiographic analysis in male C57BL/6J and NZO/BomHIDife (NZO) mice cohorts (n=10 per group) in the 6th, 12th, 18th, and 22nd week of age. Because the related mouse strains NZW/LacJ

and NZB/BlNJ are known to display autoimmune abnormalities, leading to glomerulonephritis and lupus, we choose to investigate the cardiopulmonary phenotype of NZO mice compared with healthy C57BL/6J controls. All mice underwent weekly body weight monitoring and blood glucose measurements, collected by tail incisions, using a Contour XT glucose meter (Bayer Health Care, Leverkusen, Germany). One NZO mouse died for unknown reasons in living week 20. After final echocardiography, blood samples and organs were collected for histopathological analyses.

Additional mice cohorts of C57BL/6J (n=30) and NZO (n=39) were used to perform histopathological analyses of the AoVs, invasive biventricular hemodynamic measurements, lung ultrasound, and AoV echocardiography. For each individual experiment, the number of mice used is indicated in brackets.

Echocardiography and Image Analyses

Echocardiography of both ventricles, aorta, and lung was performed using a Vevo 3100 high-resolution Imaging System coupled to a MX400 ultra-high-frequency linear array transducer (18–38 MHz; center transmit: 30 MHz; axial resolution: 50 µm) (both FUJIFILM VisualSonics, Toronto, Ontario, Canada), as described previously.[22,23] Briefly, mice were exposed to 3% isoflurane (Baxter International, Deerfield, IL) and fixed in a dorsal position on a heating pad to maintain physiological body temperatures.

Assessment of AoVs and 3-dimensional echocardiography of the aortic arch were performed using the MX700 ultra-high-frequency linear array transducer (30–70 MHz; center transmit: 50 MHz; axial resolution: 30 µm; FUJIFILM VisualSonics). The 3-dimensional image acquisition was realized with a specialized 3-dimensional motor (FUJIFILM VisualSonics), allowing for automated stepwise movement of the probe, as described previously by us.[22] All acquired images were digitally stored in raw format (DICOM) for further offline analyses. Image analyses were performed by a trained expert in small animal echocardiography using the dedicated software package VevoLAB Version 3.1.0 (FUJIFILM VisualSonics).

Hemodynamic Assessment of Pressure Profiles

LV and RV pressure profiles were recorded by invasive hemodynamic monitoring. In brief, animals were anaesthetized by intraperitoneal injection of ketamine (120 µg/g body weight) and xylazine (16 µg/g body weight), and anesthetic depth was regularly monitored by checking the toe pinch reflex. The external jugular vein and common carotid artery were exposed, and a 1F microtip pressure catheter (Millar, Houston, TX) was sequentially introduced into each vessel and advanced into the respective ventricle. Stable pressure profiles were recorded for at least 2 minutes and analyzed by Labchart software (ADInstruments, Sydney, Australia). Throughout the procedure, animals were temperature controlled via a rectal probe and heating pad. After completion of the measurements, animals were euthanized by cervical dislocation.

Histology and Histopathological Analyses

Paraffin sections of hearts and lungs (4-µm slices) were processed for immunohistochemistry. Whole hearts of neonatal pups, C57BL/6J mice, and NZO mice in the 22nd week of age were harvested for histopathological examination of AoVs in short-axis view. Samples were fixed for 24 hours in 4% formalin (Thermo Scientific, Waltham, MA) and stored in 70% ethanol. After microdissection of aortic roots, tissue samples were embedded in Tissue-Tek OCT compound (Sakura Finetek, Alphen aan den Rijn, the Netherlands), frozen in 2-methylbutane (Thermo Scientific), cooled with dry ice, and sectioned into 6-µm slices. Special care was taken that AoVs were kept intact to ensure best quality for histological analyses. Samples were stained with hematoxylin and eosin to visualize anatomic and morphologic structure of AoVs. Longitudinal cross-sections of AoVs from C57BL/6J and NZO mice were used for picrosirius red, Alizarin red, and Movat pentachrome staining. For overview images, longitudinal and cross-sectional heart slides and lungs were scanned using a MIRAX scanner (Zeiss, Ulm, Germany), which allows us to obtain digitized images of whole stained organ sections (scale, 2 mm). Quantification of images was performed using the image analysis tool from Zeiss ZEN 3.0 (blue edition) software, calculating the tissue area in pixel^2 and the percentage of stained area from total tissue area.

Statistical Analysis

Results are shown as mean±SEM with individual scatters. Statistical analyses were performed using unpaired Student t test, Mann-Whitney test (in which case data are displayed as median with interquartile range), repeated-measures ANOVA, or 2-way ANOVA with Bonferroni multiple-comparisons test as appropriate. A $P<0.05$ was assumed as statistically significant. After corroborating Gaussian distribution of the data by using the Shapiro-Wilk normality test, correlation of cardiovascular metrices was tested with the Pearson correlation coefficient (r). All analyses were performed using GraphPad Prism 7 (GraphPad Software, La Jolla, CA).

RESULTS

Early-Onset LV Failure and Structural LV Remodeling in NZO Mice

On normal chow diet, NZO mice developed a pronounced metabolic phenotype, characterized by

morbid obesity and increased serum triglyceride levels at physiological blood glucose levels (Figure S1). Serial echocardiographic monitoring of individual animals illustrates the deterioration of LV function over time in NZO mice (Figure 1A): when compared with age-matched C57BL/6J controls, NZO mice showed signs of LV hypertrophy, evident as increased LV wall thickening, LV mass, and heart-weight/tibia length ratios at 6 (LV mass) and 12 weeks of age (Figure 1B and 1C and Table 1). LV function was reduced relative to C57BL/6J controls, as indicated by a lower ejection fraction from 12 weeks of age onwards and a decrease in cardiac index after 18 weeks (Figure 1D and 1E). LV dilatation in NZO mice was evident as increased LV end-diastolic volume at 18 and 22 weeks of age, whereas LV wall thickness remained unchanged (Table 1). Because LV dilatation typically results from increased cardiac afterload,[24] we next assessed relevant hemodynamic parameters of LV contractility, relaxation, and LV pressure profiles (Figure 1F and Table 2). LV pressures were found supraphysiological in NZO mice, with end-systolic pressures elevated in all measured NZO mice, and end-diastolic pressures showing a similar albeit less consistent trend, with pressures in 3 of 8 NZO mice markedly exceeding the highest end-diastolic pressure measured in C57BL/6J controls. The notion of maladaptive LV remodeling was further supported by the results of postmortem histopathological analyses of cardiac cross-sections, demonstrating extensive thickening of the heart, an increase in total collagen content, and fibrotic lesions, with regions of CD68-positive macrophage infiltration in the LVs of NZO mice (Figure 1G through 1I).

DAVD in NZO Mice

To test for a valve defect in NZO mice, we imaged the AoVs of NZO mice and C57BL/6J controls from a parasternal short-axis view at the valve level with high-resolution echocardiography (Figure 2A). In C57BL/6J but also in NZO mice, we could clearly discern 3 individual leaflets of the AoV. Yet, in comparison to the 3 symmetrically arranged and physiologically inconspicuous leaflets in C57BL/6J mice, we detected 2 severely thickened and a third less prominent leaflet in NZO mice. Consistently, postmortem histological analyses revealed irregularly structured, degenerative AoV in NZO mice that diverted markedly from the physiological morphology with orderly structured valvular endothelium and stroma in C57BL/6J AoV (Figure 2B). In all NZO mice, 1 of the 3 valve leaflets was markedly smaller in size and dysplastic or atrophic at 22 weeks of age. NZO AoVs showed progressive thickening with abundant valvular stroma. The penetrance of extensive valve thickening and abnormal valve morphology was found as moderate to severe in 83% of male NZO mice at the age of 22 weeks (Figure 2C). Compared with male NZO mice, female NZO mice presented with similar histopathological changes of AoV leaflets, but with decreased penetrance of abnormal valve morphology (13% versus 83% moderate or severe, respectively; Figure S2). Compared with normal C57BL/6J control valves (Figure 2D), NZO mice showed mild endothelial hyperplasia (Figure 2E), moderate extracellular or intrahistiocytic stromal thickening with siderocalcinosis (Figure 2F), and multifocal cartilaginous metaplasia of the valvular stroma (Figure 2G). Quantitative assessment of mean valve area substantiated extensive valve thickening in all examined NZO mice in living week 22 compared with age-matched C57BL/6J mice (Figure 2H). NZO mice showed mild valvular calcifications by Alizarin Red staining in living week 34 (Figure S3) that was accompanied by an increase in proteoglycan content in Movat pentachrome (Figure 2I) and paralleled by decreased collagen content in picrosirius red staining (Figure 2J). These results indicate a rapidly progressing degenerative process and increased AoV stiffening, resulting in manifest AoV disease in NZO mice.

Congenital Malformation in AoVs of NZO Mice

Next, we aimed to investigate whether the AoV phenotype of adult NZO mice is caused by congenital malformation or develops as a consequence of rapid disease progression driven by environmental factors. Exemplary images from hematoxylin and eosin–stained AoVs of neonatal C57BL/6J and NZO mice demonstrate the presence of abnormal AoV thickening (black arrows) and asymmetric valve anatomy (red arrows) in NZO mice already shortly after birth when compared with C57BL/6J controls (Figure 3A), indicating congenital malformation and abnormal valvulogenesis as the underlying mechanism for valvular heart disease in NZO mice. To characterize the abnormal valve morphology in NZO mice in greater detail, we stained AoVs for periostin, a marker of valve primordial differentiation and maturation.[25,26] Our results indicate increased periostin expression in AoVs of young NZO mice (3 weeks) and older NZO mice (22 weeks) compared with C57BL/6J controls (Figure 3B, upper panel), suggesting that increased periostin expression may constitute a congenital effect rather than a sign of disease progression. In contrast, we found SRY-Box Transcription Factor 9 (Sox9), a marker of cartilage formation that is expressed during heart valve development,[27,28] to be increased as a function of age in NZO mice (Figure 3B, bottom panel). These results indicate that AoV disease in adult NZO mice is initially caused by congenital malformation and subsequently progresses further with age.
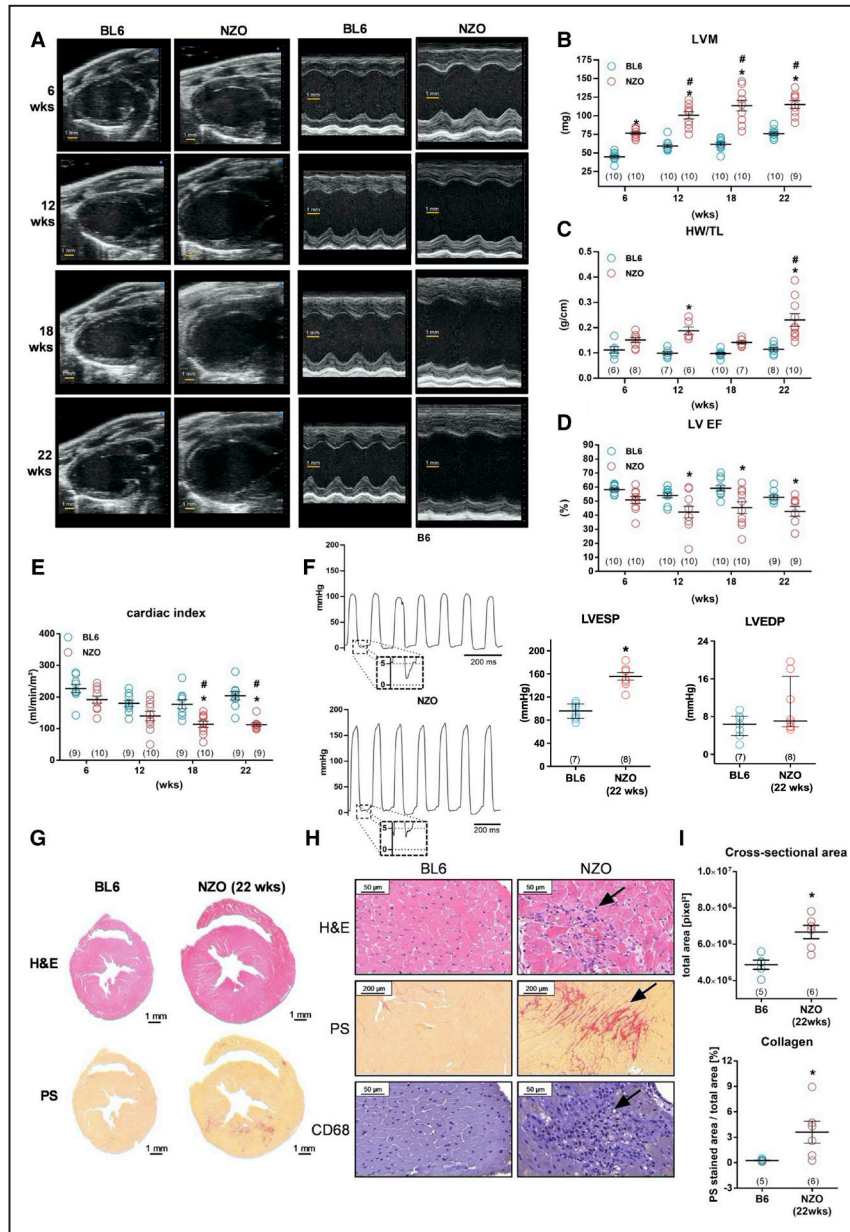
Figure 1. Onset and progression of left ventricular (LV) failure in New Zealand obese (NZO) mice.

A, Representative serial echocardiographic B- and M-mode images of the LV, originating from the same animal over time. **B** through **F**, Echocardiographic assessed LV mass (LVM; **B**), heart weight/tibia length (HW/TL) ratio (**C**), LV ejection fraction (EF; **D**), and LV cardiac index (**E**) from C57BL/6J (BL6) and NZO cohorts. In addition, LV end-diastolic pressure (LVEDP; **F**) and LV end-systolic pressure (LVESP; **F**) were assessed by microtip catheters (presented as median±interquartile range). **G**, Exemplary hematoxylin and eosin (H&E)– and picrosirius (PS) red–stained cardiac cross-sections from age-matched cohorts. **H**, Cardiac regions showing cell infiltration (upper panel), fibrotic areas (middle panel), and presence of CD68+-cell (lower panel). **I**, Quantitative analyses of cardiac cross-sectional area and PS-stained total collagen content in age-matched animal cohorts. Total numbers are indicated in parentheses. Data are presented as mean±SEM. *P<0.05 vs age-matched BL6 controls, #P<0.05 vs baseline measurement at the age of 6 weeks (wks).

DAVD Is Associated With AS, Regurgitation, and Dilatation

Consistent with the notion that pathologic valve morphology causes turbulent blood flow, which may result in structural and functional abnormalities of the thoracic aorta,[29] pulsed-wave–Doppler cine loops of the ascending aorta revealed peak velocities >3 m/s in 30% to 60% of NZO mice (depending on time point), starting at the 12th week of age, a finding that is indicative of moderate-to-high grade AS (Figure 4A through 4C). Aortic regurgitation (AR), evident as holodiastolic flow reversal, was observed in both the ascending and

Table 1. Echocardiographic Parameters of LV Function in NZO Mice as a Function of Age

Parameter	6 wk		12 wk		18 wk		22 wk	
	C57BL/6J mice	NZO mice	C57BL/6J mice	NZO mice	C57BL/6J mice	NZO mice	C57BL/6J mice	NZO mice
Total No.	10	10	10	10	10	10	10	9
HR, bpm	523±13	460±11	455±10	487±10	430±16*	473±28	494±16	499±17
LV function								
ESV, μL	17.4±1.1	37.8±2.6	27.7±1.4	55.7±5.6†	26.7±1.9	52.2±7.5†	35.2±2.1	56.6±8.3†
EDV, μL	41.5±2.6	76.7±2.8†	60.5±2.7	95.8±6.1†	65.2±3.1*	91.6±6.9†	73.5±3.2*	95.5±7.6
EF, %	58.2±1.0	50.9±2.5	54.1±1.7	42.3±4.1†	59.2±2.1	45.4±4.2†	52.2±1.5	42.7±3.5†
SV, μL	24.2±1.7	38.9±2.3†	32.9±1.9	40.2±4.4	38.5±2.0*	39.4±2.4	38.3±1.8*	38.9±1.4
CO, mL/min	12.8±1.0	17.9±1.1	14.9±0.8	19.4±2.0	16.6±1.1	18.6±1.5	18.9±1.1	19.4±1.1
LV dimension								
LVM, mg	44.8±1.8	76.6±1.8†	59.3±2.4	100.7±4.8*†	61.8±2.4	113.6±7.2*†	76.0±2.0*	115.2±5.2*†
LVID,d, mm	3.61±0.06	4.26±0.06†	3.97±0.1	4.60±0.13†	3.96±0.07	4.66±0.14†	4.38±0.06*	4.83±0.13*
LVAW,d, mm	0.52±0.01	0.64±0.01†	0.58±0.01	0.71±0.01†	0.59±0.02	0.76±0.02*†	0.61±0.01*	0.75±0.03*†
LVPW,d, mm	0.51±0.01	0.62±0.01†	0.55±0.01	0.70±0.01*†	0.59±0.01*	0.75±0.02*†	0.59±0.01*	0.72±0.02*†

Data are represented as mean±SEM. Bpm indicates beats per minute; CO, cardiac output; EDV, end-diastolic volume; EF, ejection fraction; ESV, end-systolic volume; HR, heart rate; LV, left ventricular; LVAW,d, diastolic LV anterior wall; LVID,d, diastolic LV inner diameter; LVM, LV mass; LVPW,d, diastolic LV posterior wall; NZO, New Zealand obese; and SV, stroke volume.

*$P<0.05$ vs corresponding 6 weeks baseline control group.

†$P<0.05$ vs corresponding C57BL/6J control group.

Table 2. Hemodynamics in C57BL/6J and NZO Mice at 22 Weeks of Age

Variable	C57BL/6J mice	NZO mice
Total No.	7	8
LV hemodynamics		
LVESP, mm Hg	92.9±4.8	155.8±6.6*
LVEDP, mm Hg	6.1±0.1	10.1±2.1
dP/dt$_{max}$, mm Hg/s	8769±1078	9929±449
dP/dt$_{min}$, mm Hg/s	−8743±1372	−10 376±753
τ, ms	7.4±0.5	9.8±1.9
Total No.	5	8
RV hemodynamics		
RVSP, mm Hg	21.5±0.6	36.2±1.7*
RVEDP, mm Hg	0.8±1.7	5.7±0.8*
dP/dt$_{max}$, mm Hg/s	1588±294	2670±251*
dP/dt$_{min}$, mm Hg/s	−918±100	−2738±389*
τ, ms	16.0±5.4	10.8±1.9

Data are represented as mean±SEM. dP/dt$_{max}$ indicates maximum rate of pressure change; dP/dt$_{min}$, minimum rate of pressure change; LV, left ventricular; LVEDP, LV end-diastolic pressure; LVESP, LV end-systolic pressure; NZO, New Zealand obese; RV, right ventricular; RVEDP, RV end-diastolic pressure; RVSP, RV systolic pressure; and τ, time constant of active relaxation.

*$P<0.05$ vs C57BL/6J control group.

descending aorta and quantified as amount of backwards flowing blood (toward the left heart) per minute (Figure 4A, right panel, 3-dimensional). In line with a high prevalence of AS in NZO mice, 75% of NZO showed significant AR at the 22nd week of age, defined as flow reversal >5 mL/min. The degree of AS correlated with key parameters of echocardiographic-assessed LV function, in line with a physiologic link between aortic flow profiles and LV outcome (Figure 4E). In accordance with the European Association of Echocardiography/American Society of Echocardiography recommendations, aortic peak velocity was used for simplified classification of AS severity.[30] Functional severity of AS was heterogeneous among NZO mice. Accordingly, 41% of NZO mice showed no signs of hemodynamic relevant AS, whereas 6% had AS I, 24% had AS II, and 29% presented with AS grade III (Figure 4F). When stratifying hemodynamic data from NZO mice, which received echocardiographic and hemodynamic examination for AS severity, mice with moderate or severe AS displayed significantly higher LV end-diastolic pressures compared with NZO mice with no or mild AS, demonstrating increased LV afterload in moderate and severe AS (Figure 4G). Over time, DAVD was also associated with altered aortic morphology: serial 2-dimensional monitoring of the thoracic aorta revealed a dilatation of the ascending aorta, whereas other parts of the aortic arch remained unchanged over time

(Figure 4H, data not shown). Aortic dilatation was further confirmed by novel multidimensional echocardiography, which revealed increased aortic volumes in NZO mice compared with C57BL/6J mice (Figure 4I and Videos S1 and S2). Overall, these data identified hemodynamic relevant AS, regurgitation, and ascending aortic dilatation subsequent to DAVDs in NZO mice.

LV Failure Is Associated With PH and Ultimately RV Failure

Because secondary PH and RV failure have been linked to AS and left-sided valve disease, we next analyzed RV function in NZO mice.[31] Echocardiographic RV mass in NZO mice exceeded RV mass in C57BL/6J mice at all time points (Figure 5A), whereas the ratio of RV mass/LV mass remained unchanged (Figure S4A). Concomitantly, RV inner diameter increased over time in NZO yet not in C57BL/6J mice (Figure 5B) and notably more so than LV inner diameter (Table 1 and Figure S4B). These findings suggest that dilated cardiomyopathy progresses faster in the RV compared with the LV, a result that is in line with clinical studies that identified RV failure as independent prognostic value for adverse outcome in LV disease.[32] Increased RV afterload and impaired RV function were further substantiated by echocardiographic and *postmortem* analyses, showing reduced tricuspid annular plane systolic excursion, RV ejection fraction, pulmonary artery acceleration and ejection times, and an increased RV weight/tibia length ratio (Figure 5C through 5F and Table 3). Invasive hemodynamic measurements of RV systolic pressure identified markedly elevated RV systolic pressure values >30 mm Hg in 6 of 8 tested NZO mice (Figure 5G and Table 2). Of note, 2 NZO mice had to be excluded from RV systolic pressure measurements because of excessive congestion of the external jugular vein, preventing proper catheter insertion. Finally, RV function, assessed as RV ejection fraction and tricuspid annular plane systolic excursion, correlated inversely with the degree of aortic regurgitation and AS, suggesting AoV degeneration as important driver of PH in NZO mice (Figure 5H).

Lung Congestion and Vascular Remodeling

In addition to the effects on pulmonary and RV hemodynamics, we tested for echocardiographic signs of lung congestion in NZO mice. Starting in living week 18 (ie, the earliest time point associated with RV dysfunction), B-lines, pleural thickening, and reduced lung sliding could be detected as characteristic symptoms
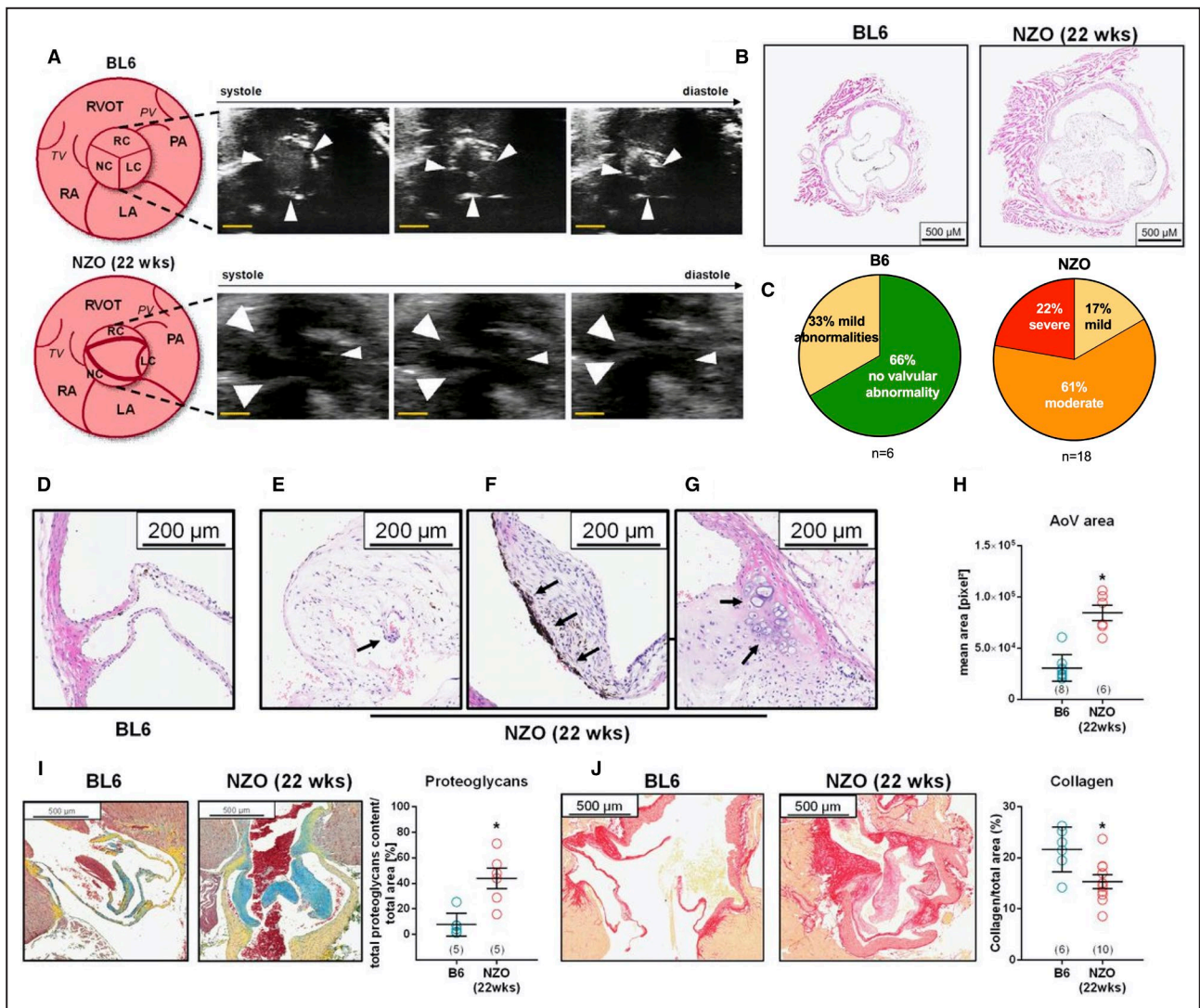
Figure 2. Siderocalcinosis and multifocal cartilaginous metaplasia in aortic valves (AoVs) of New Zealand obese (NZO) mice.
A, Schematic overview of a parasternal short-axis view at the aortic valve level and corresponding high-resolution echocardiographic B-mode images of AoVs in NZO and age-matched C57BL/6J (BL6) mice. White arrows indicate leaflets. B, Hematoxylin and eosin–stained cross-sections of AoVs in a short-axis view at 2.5-fold magnification. C, Semiquantitative analyses of AoV thickening and abnormal valve morphology in age-matched BL6 and NZO mice (both 22 weeks). D, The ×20 magnification indicated physiologic aortic valve morphology in BL6 mice compared with pathophysiological endothelial hyperplasia (E), stromal thickening with siderocalcinosis (F), and multifocal cartilaginous metaplasia (G) in age-matched NZO mice. H, Quantification of AoV mean area in BL6 and NZO mice at 22 weeks of age. I, Longitudinal cross-sections of the aortic valve stained with Movat pentachrome stain (MPS) and (J) picrosirius (PS) red with corresponding quantitative analyses of proteoglycans (stained blue, MPS) and collagen content (stained red [SR]), respectively. Total numbers are indicated in parentheses. Data are presented as mean±SEM. LA indicates left atrium; LC, left coronary leaflet; NC, noncoronary leaflet; PA, pulmonary artery; PV, pulmonary valve; RA, right atrium; RC, right coronary leaflet; RVOT, right ventricular outflow tract; TV, tricuspid valve; and wks, weeks. *$P<0.05$ vs age-matched BL6 controls.

of lung congestion[33] in most NZO mice (Figure 6A and Videos S3 and S4), resulting in a marked elevation of the mouse lung ultrasound score for lung congestion in NZO mice compared with C57BL/6J mice. Finally, we tested whether lung congestion in NZO mice caused reactive lung vascular remodeling as indicator for the progression from isolated postcapillary PH to combined postcapillary and precapillary PH.[34] Compared with

C57BL/6J controls, NZO mice had normal (20–50 μm vessels) or even slightly reduced mean medial wall thickness (50–150 μm vessels), and muscularization of small pulmonary microvessels did not differ between NZO and C57BL/6J mice (Figure 6B through 6D). That notwithstanding, lung fibrosis was evident as an increase in picrosirius red–stained total collagen I and III in lungs of NZO compared with C57BL/6J mice (Figure 6E).
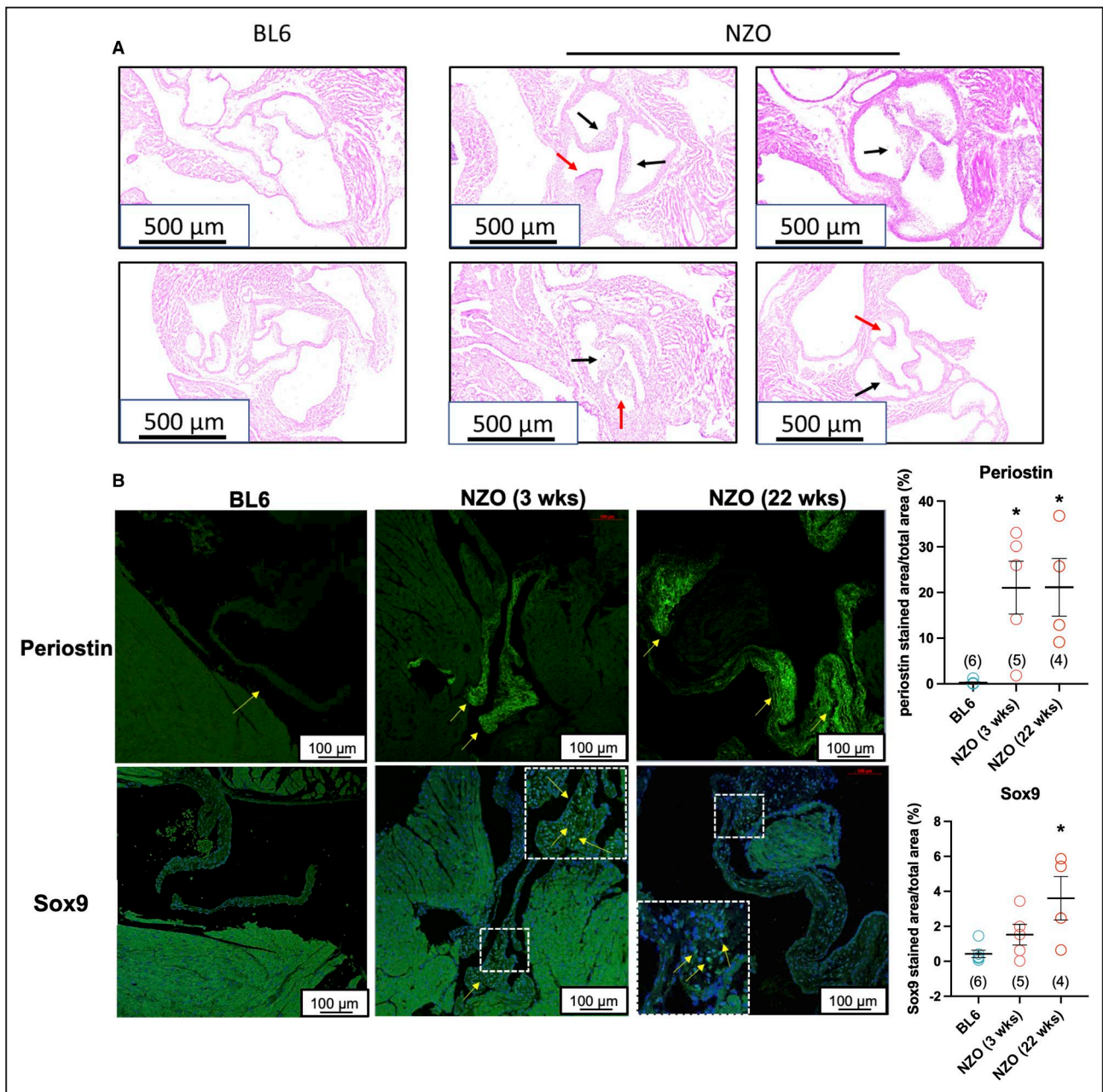
Figure 3. Congenital malformation as the underlying cause of aortic stenosis in New Zealand obese (NZO) mice.
A, Exemplary images of hematoxylin and eosin–stained aortic valves from neonatal C57BL/6J (BL6) and NZO mice (<3 days after birth), indicating aortic valve thickening (black arrows) and asymmetric leaflet formation (red arrows) in NZO mice compared with BL6 controls. **B**, Exemplary images of immunofluorescence staining and corresponding quantitative analyses of periostin (upper panel) and Sox9 (lower panel) in male BL6 mice (22 weeks) and NZO mice (3 and 22 weeks). Total numbers are indicated in parentheses. Data are presented as mean±SEM. *P<0.05 vs BL6 controls.

DISCUSSION

Collectively, our results demonstrate a complex cardiopulmonary phenotype in male naïve NZO mice that originates from a progressive degeneration of the AoVs. In contrast to previously reported murine models of AS, which rely on surgical interventions or complex induction of multiple risk factors for manifest AS development,[15,16,18] NZO mice develop spontaneous AS

and may thus present a clinically relevant and versatile model for pathomechanistic and therapeutic studies of AS. The translatability of this naturally and intrinsically occurring cardiopulmonary phenotype is highlighted by the facts that NZO mice (1) carry several clinical risk factors for AS (namely, obesity and dyslipidemia), which likely trigger or promote the multifactorial disease[20,21] and (2) replicate the characteristic cardiopulmonary phenotype of clinical AS, with aortic regurgitation, LV
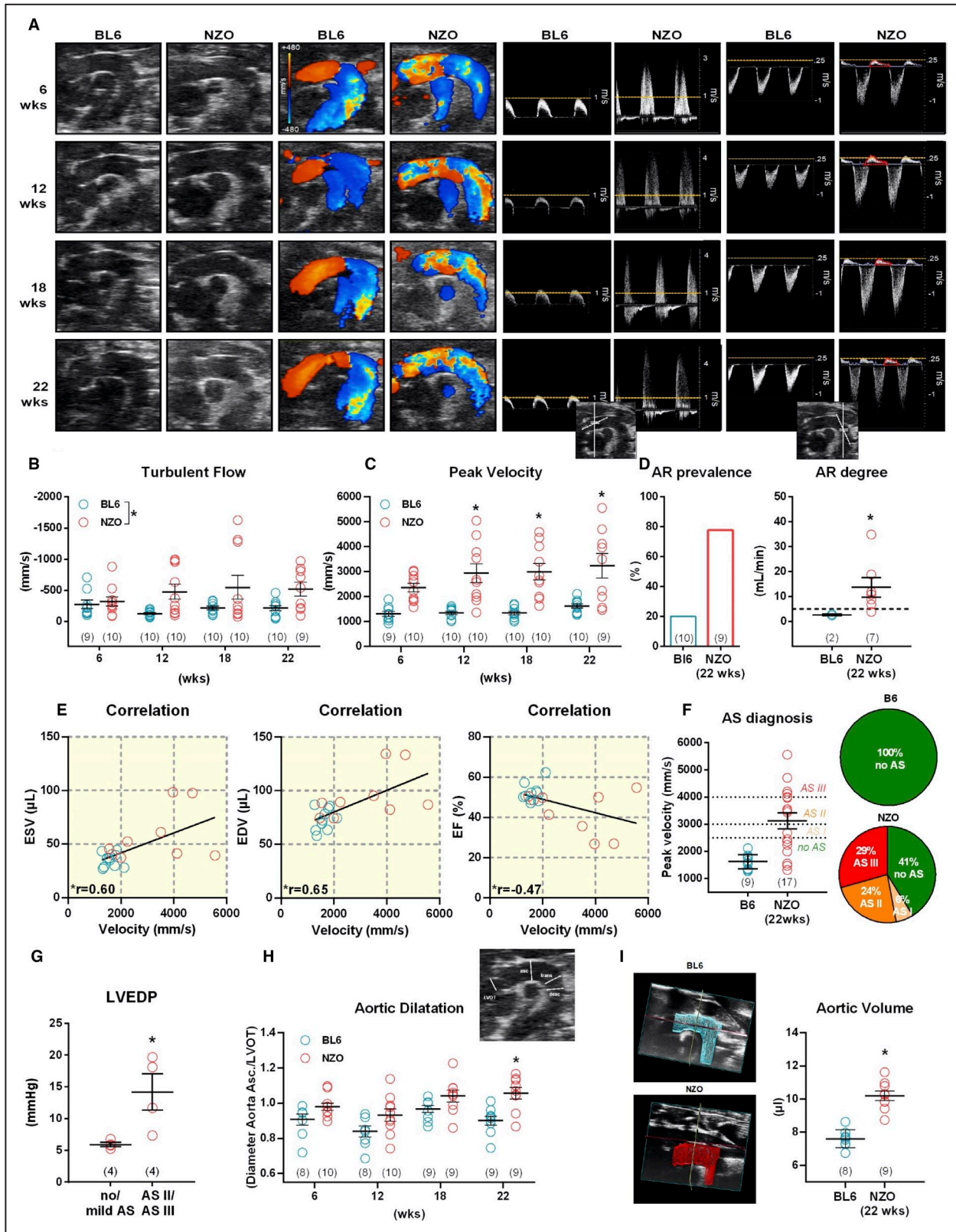
hypertrophy progressing to decompensated LV failure, PH, and ultimately RV dilation and failure.

In humans, DAVD is the most common cause of AS and considered as an active, proliferative, and progressive disease, that is accelerated by multiple risk factors similar to those associated with atherosclerotic disease.[35–37] Risk factor modifications via drug treatment and lifestyle intervention can reduce the

Figure 4.   Stromal thickening of aortic valves causes aortic regurgitation and thoracic aortopathy in New Zealand obese (NZO) mice.

A, Exemplary serial echocardiographic B-mode and color-Doppler images of the aortic arch, originating from the same animal (left panel). Pulsed-wave (PW)–Doppler–assessed velocity profiles from the ascending and descending aorta (right panel). Yellow dashed line was set as a landmark and indicates a velocity of 1 m/s in ascending aorta or 25 m/s in descending aorta. Red line highlights holodiastolic flow reversal. **B** through **D**, Quantification of turbulent flow, peak velocity profiles, and aortic regurgitation from PW-Doppler cine loops of the ascending aorta. **E**, Correlation analyses of left ventricular (LV) end-systolic volume (ESV), LV end-diastolic volume (EDV), and ejection fraction (EF) with the degree of aortic stenosis expressed as ascending aortic peak velocity in age-matched mice cohorts. **F**, Aortic stenosis (AS) severity graded according to the ascending peak velocity profile (≤2500 mm/s=no AS, 2500–3000 mm/s=AS I, 3000–4000 mm/s=AS II, and ≥4000 mm/s=AS III). **G**, LV end-diastolic pressure (LVEDP) of NZO mice, stratified by AS severity. **H**, Dilatation of the ascending aorta, defined as the ascending aortic diameter/LV outflow tract ratio. Analysis was based on 2-dimensional B-mode images of the aortic arch. **I**, Three-dimensional reconstruction of traced multidimensional echocardiographic B-mode images from the ascending aorta and related quantification of ascending aortic volumes. Total numbers are indicated in parentheses. Data are presented as mean±SEM. AR indicates aortic regurgitation; and wks, weeks. *$P<0.05$ vs age-matched C57BL/6J (BL6) controls.

incidence of AS and slow down the progressive nature of the disease process.[13] AS ranges from a relatively benign course in asymptomatic patients to a disease with high mortality rate once symptoms develop.[38] Of interest, this physiological continuum is equally evident in male NZO mice of genetically identical ancestry, in that 50% of mice present with moderate or severe AS and AR, whereas the other half only shows mild AS or no phenotype at all. Notably, this heterogeneity in AS severity directly translates into diastolic LV function in that mice with more severe AS show increased LV end-diastolic pressure values compared with littermates with no or mild AS. Our findings in NZO mice thus replicate the situation in patients, where the initial pace of the disease process may differ between individuals, yet hemodynamic changes occur rapidly and uniformly once AoV obstruction develops.[39,40] Moreover, some NZO mice displayed ventricular failure in the absence of AS, suggesting a role for hemodynamically independent factors to the cardiopulmonary phenotype of NZO mice, as described for AS pathogenesis.[41,42] Although some female mice developed abnormal AoVs with extensive thickening of valvular leaflets and reduced collagen content, similar to their male counterparts, overall penetrance of this phenotype was markedly lower in females than in males. These findings are in line with clinical data, as women are less often diagnosed with AS[43] and the corresponding fibrocalcific changes of aortic leaflets than men,[3] although, paradoxically, they tend to have a worse outcome.[44] The observed sex differences are further in line with our previous findings demonstrating that female, as opposed to male, NZO mice are protected from mitochondrial dysfunction and impaired cardiac energy metabolism.[45]

According to the clinical guidelines, echocardiography is the key diagnostic modality to confirm the presence and severity of AS and to assess the degree of ventricular dysfunction in patients.[2] The echocardiographic phenotype of NZO mice matches the clinical presentation of patients with AS, as illustrated by increased peak velocities in the ascending aorta, AR with holodiastolic flow reversal, and dilatation of the

ascending aorta, a common complication in patients with calcific AS.[46]

AS in NZO mice was not attributable to a bicuspid AoV, yet, AoVs displayed an asymmetric valve anatomy shortly after birth, a finding that is strongly associated with the future development of AS in patients.[47] Similarly, histopathological evidence for endothelial injury, cartilaginous transformation, periostin overexpression, and valvular thickening in NZO mice is closely reminiscent to similar findings in human AS, where these pathological features are considered to cause stiffening of the AoVs before the deposition of collagen and calcium.[48,49] NZO mice showed a pattern of increased proteoglycan and decreased collagen expression, indicating drastic remodeling of the valvular extracellular matrix.[50] In the steady state, AoVs are composed of 3 extracellular matrix layers: (1) collagens (fibrosa), (2) proteoglycans (spongiosa), and (3) and elastin (ventricularis). In calcific AS, proteoglycans typically become overexpressed, actively participating in lipid retention and modification.[51] An association between proteoglycan overexpression and calcified regions has also been found in human DAVD, as proteoglycans accumulate around calcified nodules in the fibrosa layer.[52,53] Particularly, small leucin-rich proteoglycans were shown to play a key role in DAVD because of their potency to interact with inflammatory molecules and immune cells and their capacity to promote lipid retention.[54]

Sox9 is known to play a key role in heart valve maturation after birth by regulating extracellular matrix proteins.[27] The finding that adult NZO mice upregulate Sox9 is unexpected as previous studies have mainly addressed the role of Sox9 during valvulogenesis,[27] yet little is known about its function in mature heart valves and potential functional consequences. Of note, increased Sox9 expression has been reported in murine models of myxomatous valve disease, which is the most common cause of mitral valve regurgitation.[55,56] In myxomatous valve disease, enhanced Sox9 expression is associated with increased proteoglycan composition.[57] Conversely, Sox9^{+/−} mice exhibit AoV
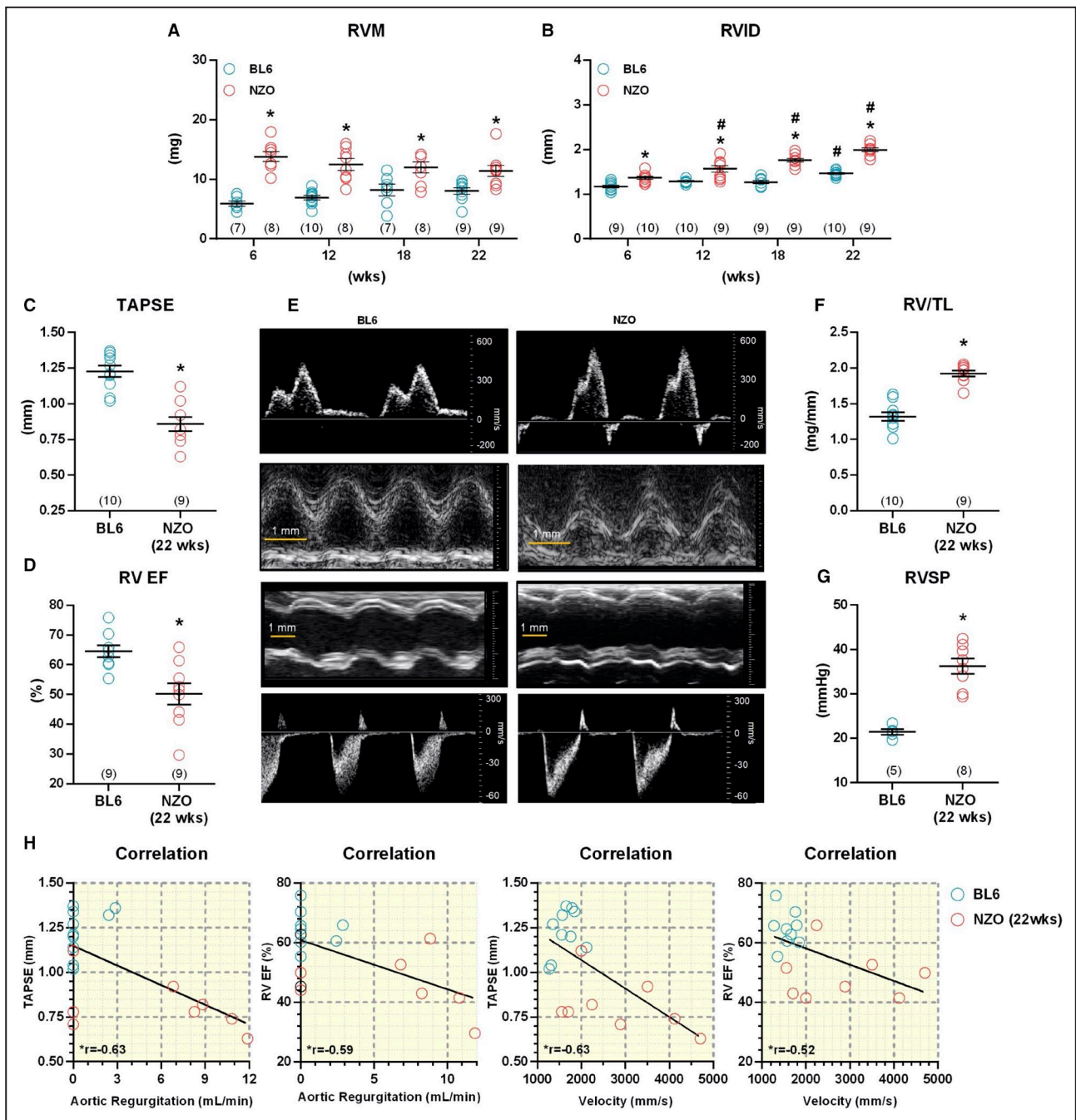
Figure 5. Pulmonary hypertension and right ventricular (RV) failure in New Zealand obese (NZO) mice.
RV mass (RVM) (**A**) and RV internal diameter (RVID) (**B**), as assessed via echocardiography, tricuspid annular plane systolic excursion (TAPSE) (**C**) and RV ejection fraction (EF) (**D**) in C57BL/6J (BL6) and NZO mice of 22 weeks of age, and representative echocardiographic images (**E**) show pulsed-wave–Doppler flow profiles of the tricuspid valve derived from a 4-chamber view (upper panel), TAPSE, originating from a 4-chamber view (upper mid), M-modes of the RV in parasternal long-axis view (lower mid), and a flow profile of the pulmonary artery assessed from a parasternal short-axis view on the valve level (bottom panel) in BL6 and NZO mice of 22 weeks of age. RV weight/tibia length (TL) (**F**) and RV systolic pressure (RVSP) (**G**), as measured by RV catheterization in BL6 and NZO mice. **H**, Correlation analyses of RV function to the degree of aortic stenosis and regurgitation. Total numbers are indicated in parentheses. Data are presented as mean±SEM. *$P<0.05$ vs age-matched BL6 controls, #$P<0.05$ vs baseline measurement at sixth week of age.

calcification associated with reduced proteoglycan expression.[58] Proper proteoglycan expression is crucial for the regular function and integrity of mature valvular leaflets,[59] highlighting an important role for Sox9 in maintaining physiologic valvular tissue composition. Sox9 dysregulation in NZO mice may therefore have profound effects by promoting proteoglycan-related valvular heart disease associated with valve stiffening.

Table 3. Echocardiographic Parameters of RV Function at 22 Weeks of Age

Variable	C57BL/6J mice	NZO mice
Total No.	10	9
RV dimension		
RVID, d, mm	1.45±0.02	1.99±0.04*
RVAW, d, mm	0.39±0.01 (9)	0.44±0.02*
RVID/LVID	0.33±0.01	0.42±0.01*
RV function		
IVCT, ms	17.7±1.9 (8)	25.7±0.9*
E-wave amplitude, mm/s	285.6±28.3 (8)	265.0±34.6
A-wave amplitude, mm/s	437.8±38.9 (8)	471.5±37.6
E/A ratio	0.65±0.03 (8)	0.52±0.05* (8)
RIMP	0.36±0.03 (8)	0.57±0.04* (6)
TAPSE, mm	1.23±0.04	0.86±0.05*
EF, %	64.6±2.0 (9)	50.2±3.6
PV measurements		
PAT, ms	24.4±1.04	20.4±0.7*
PET, ms	92.5±2.5	76.6±3.3*
PAT/PET ratio	0.27±0.01	0.27±0.01
Peak velocity, mm/s	−687.1±21.8	−676.2±38.6
PA VTI, mm	31.4±1.4	26.9±2.0

Numbers in parentheses indicate numbers of analyzed images, when different from animal number. Total numbers may diverge because of occasionally poor image quality. Data are represented as mean±SEM. A indicates late diastolic filling; E, peak early filling; EF, ejection fraction; IVCT, isovolumetric contractility time; LVID, left ventricular inner diameter; NZO, New Zealand obese; PA VTI, pulmonary artery velocity time integral; PAT, pulmonary acceleration time; PET, pulmonary ejection time; PV, pulmonary vascular; RIMP, RV index of myocardial performance; RV, right ventricular; RVAW, d, diastolic RV anterior wall; RVID, d, diastolic RV inner diameter; and TAPSE, tricuspid annular plane systolic excursion.

*$P<0.05$ vs C57BL/6J control group.

In contrast to increased Sox9 expression, elevated periostin expression is already present in young NZO mice and may indicate a congenital defect and early disease manifestation rather than a disease progression. Periostin regulates collagen fibrillogenesis,[60] and its overexpression results in increased matrix compaction,[61] highlighting periostin as a mediator of matrix remodeling toward a mature valve structure during valvulogenesis. In line with this concept, data from histopathological findings in human AoVs show periostin expression to be strikingly upregulated and expanded in adult patients with atherosclerotic and rheumatic valvular heart disease.[62] Altogether, impaired Sox9, periostin, and proteoglycan expression patterns point toward dysregulated protein composition and impaired extracellular matrix maturation in NZO mice compared with C57BL/6J controls, which might be a core mechanism for the development of AS in NZO mice.

Clinically, AS and the subsequent emergence of aortic regurgitation trigger the hemodynamic propagation of the disease process via increased LV pressure and volume, resulting in the development of left-sided valvular heart disease. The characteristic features of this process, such as increased myocardial cell mass, interstitial fibrosis, and echocardiographic evidence of LV failure, are equally evident in NZO mice.[46] As LV failure progresses, LV diastolic function declines, as evident by LV end-diastolic dilatation and increase in τ, resulting in increased LV preload (LV end-diastolic pressure) and congestive heart failure with progressive transmission of elevated hemodynamic pressures from the LV to the left atrium and into the lung, where congestive pulmonary edema can be detected by lung ultrasound. In some clinical cases, the pulmonary vasculature adapts to these elevated hemodynamic pressures by extensive remodeling of the vascular intima, media, and perivascular interstitium, thus further aggravating right-sided heart afterload via a combination of pre-capillary and postcapillary PH.[63] Ultimately, postcapillary PH or combined precapillary and postcapillary PH result in progressive RV dilatation and failure, as demonstrated by the progressive increase in RV inner diameter and reduced RV ejection fraction. Although this pathophysiological sequence is well established in humans and recapitulated in rat or guinea pig models of aortic banding,[64,65] similar models in mice produced a less pronounced pulmonary phenotype with moderate pulmonary vascular remodeling.[66] The findings in NZO mice are in line with these reports in that there was a similar trend for increased small pulmonary artery muscularization compared with C57BL/6J mice, which, however, failed to reach the level of significance. That notwithstanding, NZO mice present, to our knowledge, the first murine model of spontaneous PH with left-sided heart disease and metabolic syndrome, mimicking another highly prevalent yet poorly understood clinical scenario.[67]

Although we provide, to our knowledge, the most extensive echocardiographic assessment of DAVD, AS, and associated end-organ damages in a murine model to date, our data set is at the same time restricted to the technical limitations of small animal echocardiography. This notion refers specifically to the calculation of AoV area using the continuity equation, which is the standard of care for the assessment of AS severity in humans.[2,30] AoV area calculations become important when aortic velocity profiles are higher than normal (eg, coexisting AR) or lower than normal (eg, LV dysfunction) as transaortic velocities and gradients vary with volumes.[46] Unfortunately, AoV area measurements/calculations are presently not feasible in mice because of the deficiency of continuous-wave Doppler ultrasound technique in small animal ultrasound devices, a technique that is highly recommended for the precise assessment of valve stenosis in clinical practice.[30] As a result, diagnosis of AS in murine models is
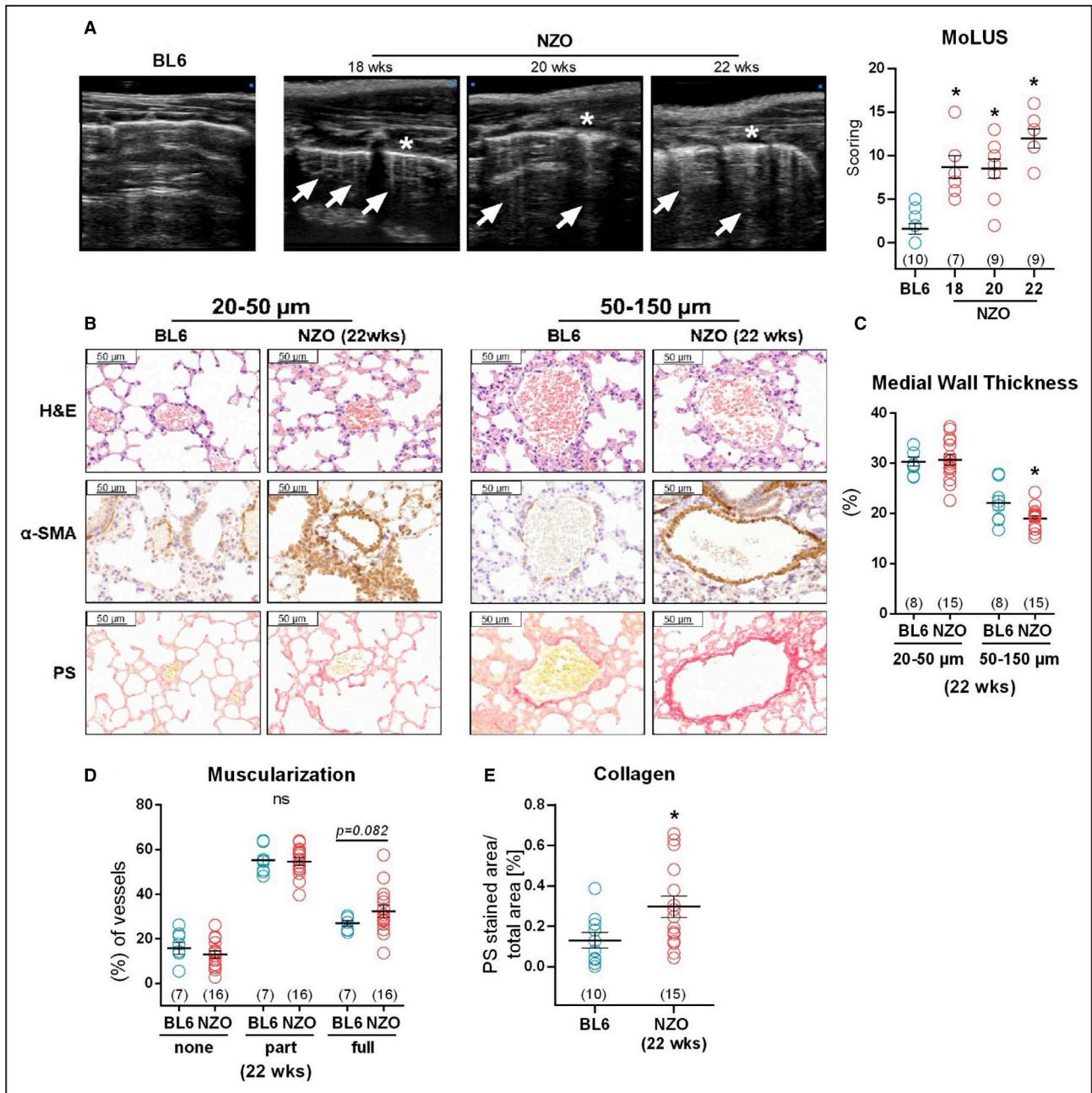
Figure 6. Lung congestion and fibrosis in New Zealand obese (NZO) mice.
A, Exemplary lung ultrasound images of the right lung from C57BL/6J (BL6) and NZO mice at different ages with corresponding semiquantitative mouse lung ultrasound (MoLUS) scores indicating congestive pulmonary edema in NZO compared with BL6 mice. Arrows indicate emerging B-lines, and asterisks indicate pleural thickening. **B**, Representative images of hematoxylin and eosin (H&E)–stained (upper panel), α-smooth muscle actin (α-SMA)–stained (middle panel), and picrosirius (PS) red–stained (lower panel) lung vessels stratified by vessel diameters ranging from 20 to 50 and 50 to 150 μm. **C**, Corresponding quantification of vascular wall thickness relative to vessel diameter (=medial wall thickness) in H&E-stained lung microvessels of 20 to 50 and 50 to 150 μm diameter. Semiquantitative analysis of none, partially, and fully muscularized α-SMA–stained lung microvessels (20–50 μm diameter) (**D**) and quantitative analysis of PS-stained lung sections (**E**), indicating the fraction of total collagen positive area over total lung tissue. Total numbers are indicated in parentheses. Data are presented as mean±SEM. *$P<0.05$ vs age-matched BL6 controls.

presently restricted to the measurement of aortic velocity profiles, which may lead to false-negative results. Notably, in the present study, this might have led to an underestimation of AS incidence and severity in NZO mice.

CONCLUSIONS

Herein, we report, to our knowledge, a novel murine model that spontaneously develops DAVD and AS at an early age. The resulting complex cardiopulmonary

phenotype in NZO mice closely mimics the corresponding clinical scenario in patients, attesting to the high translatability of this commercially available model for studies of DAVD and AS as well as the associated cardiopulmonary end-organ damage. This new research tool paves the way for the detailed investigation of molecular and morphological mechanisms underlying AS and may serve as a platform for the testing of novel drug targets and treatment strategies.

ARTICLE INFORMATION

Received July 5, 2021; accepted October 20, 2021.

Affiliations

Department of Molecular Toxicology, German Institute of Human Nutrition, Potsdam-Rehbruecke, Germany (C.O., C.J., T.G.); German Centre for Cardiovascular Research (partner site Berlin), Berlin, Germany (C.O., K.P., N.H., C.J., S.J., J.H.L., S.V.L., U.K., T.G., W.M.K., J.G.); Berlin Institute of Health Center for Regenerative Therapies and Berlin-Brandenburg Center for Regenerative Therapies (K.P., S.V.L.), Institute of Physiology (N.H., J.H.L., W.M.K., J.G.), Department of Cardiology (S.V.L.) and Center for Cardiovascular Research/Institute of Pharmacology (U.K., J.G.), Charité–Universitätsmedizin Berlin, Berlin, Germany; Department of Medicine/Cardiology (S.J.) and Department of Anesthesiology (J.K.), Deutsches Herzzentrum Berlin, Berlin, Germany (S.J.); Max-Delbrück Center for Molecular Medicine in the Helmholtz Association, Berlin, Germany (S.J.); Center for Systems Biology, Massachusetts General Hospital and Harvard Medical School, Boston, MA (C.S.M., Y.I., F.S., M.N., J.G.); Department of Veterinary Pathology, Freie Universität Berlin, Berlin, Germany (R.K.); German Center for Diabetes Research, München-Neuherberg, Germany (T.G.); Institute of Nutritional Science, University of Potsdam, Nuthetal, Germany (T.G.); and Departments of Surgery and Physiology, University of Toronto and Keenan Research Centre for Biomedical Science of St. Michael's, Toronto, Canada (W.M.K.).

Acknowledgments

We are thankful to our colleague Stefanie Deubel (Molecular Toxicology Department, German Institute of Human Nutrition) for assisting in all animal experiments and Elisabeth Meyer (Max-Rubner Laboratory German Institute of Human Nutrition) for preparing the tissue slides for histology. Furthermore, we thank Katrin Ritter (Central Regulation of Metabolism Department, German Institute of Human Nutrition), who measured the triglyceride levels in the plasma samples.

Sources of Funding

Drs J. Grune, Kuebler, T. Grune, and Ott were supported by DynAge and Freie Univerität Berlin. Drs Ott, J. Grune, and T. Grune were supported by the German Center for Cardiovascular Research (100290384 and 81Z0100501), the Gesundheitscampus Brandenburg (06-GeCa:H228-05/002/005), and T. Grune by the Deutsche Forschungsgemeinschaft (GR 1240/22-1 and BE 6400/3-1). Dr Kintscher was supported by the German Centre for Cardiovascular Research (BER 5.4 PR), the Deutsche Forschungsgemeinschaft (KI 712/10-1), and the Einstein Foundation/Foundation Charité (EVF-BIH-2018-440). Dr Kuebler was supported by the Deutsche Forschungsgemeinschaft, the Canadian Institutes for Health Research, and the Heart and Stroke Foundation of Canada. Dr J. Grune was supported by the Deutsche Gesellschaft für Kardiologie, German Centre for Cardiovascular Research, Deutsche Forschungsgemeinschaft, and Charité 3R. Dr McAlpine was supported by a Canadian Institutes of Health Research Banting Fellowship.

Disclosures

Dr Swirski is a consultant for Verseau Therapeutics. Dr Nahrendorf is a consultant for Biogen, Eli Lilly and Companym Gimv, GlaxoSmithKline, IFM Therapeutics, Sigilon, and Verseau. He has received gifts from Alnylam Pharmaceuticals, BIOTRONIK INC, and Medtronic. He has received grants from CSL Behring, GlycoMimetics, Novartis, and Pfizer Canada, Inc. Dr Kuebler has received grants from Bundesministerium für Bildung und Forschung, Deutsche Forschungsgemeinschaft, and Deutsches Zentrum für Herz-Kreislaufforschung. The remaining authors have no disclosures to report.

Supplementary Material

Data S1
Figures S1–S4
References 68–70
Videos S1–S4

REFERENCES

1. Goldbarg SH, Elmariah S, Miller MA, Fuster V. Insights into degenerative aortic valve disease. *J Am Coll Cardiol*. 2007;50:1205–1213. doi: 10.1016/j.jacc.2007.06.024

2. Baumgartner H, Falk V, Bax JJ, De Bonis M, Hamm C, Holm PJ, Iung B, Lancellotti P, Lansac E, Rodriguez Muñoz D, et al. 2017 ESC/EACTS guidelines for the management of valvular heart disease. *Eur Heart J*. 2017;38:2739–2791. doi: 10.1093/eurheartj/ehx391

3. Nkomo VT, Gardin JM, Skelton TN, Gottdiener JS, Scott CG, Enriquez-Sarano M. Burden of valvular heart diseases: a population-based study. *Lancet*. 2006;368:1005–1011. doi: 10.1016/S0140-6736(06)69208-8

4. Benjamin EJ, Blaha MJ, Chiuve SE, Cushman M, Das SR, Deo R, de Ferranti SD, Floyd J, Fornage M, Gillespie C, et al. Heart disease and stroke statistics-2017 update: a report from the American Heart Association. *Circulation*. 2017;135:e146–e603. doi: 10.1161/CIR.0000000000000485

5. Lindroos M, Kupari M, Heikkilä J, Tilvis R. Prevalence of aortic valve abnormalities in the elderly: an echocardiographic study of a random population sample. *J Am Coll Cardiol*. 1993;21:1220–1225. doi: 10.1016/0735-1097(93)90249-Z

6. Iung B, Baron G, Butchart EG, Delahaye F, Gohlke-Bärwolf C, Levang OW, Tornos P, Vanoverschelde J-L, Vermeer F, Boersma E, et al. A prospective survey of patients with valvular heart disease in Europe: the Euro Heart Survey on Valvular Heart Disease. *Eur Heart J*. 2003;24:1231–1243. doi: 10.1016/S0195-668X(03)00201-X

7. Freeman RV, Otto CM. Spectrum of calcific aortic valve disease. *Circulation*. 2005;111:3316–3326. doi: 10.1161/CIRCULATIONAHA.104.486738

8. Everett RJ, Clavel M-A, Pibarot P, Dweck MR. Timing of intervention in aortic stenosis: a review of current and future strategies. *Heart*. 2018;104:2067–2076. doi: 10.1136/heartjnl-2017-312304

9. Roselli EE, Abdel Azim A, Houghtaling PL, Jaber WA, Blackstone EH. Pulmonary hypertension is associated with worse early and late outcomes after aortic valve replacement: implications for transcatheter aortic valve replacement. *J Thorac Cardiovasc Surg*. 2012;144:1067–1074.e2. doi: 10.1016/j.jtcvs.2012.08.029

10. O'Sullivan CJ, Wenaweser P, Ceylan O, Rat-Wirtzler J, Stortecky S, Heg D, Spitzer E, Zanchin T, Praz F, Tüller D, et al. Effect of pulmonary hypertension hemodynamic presentation on clinical outcomes in patients with severe symptomatic aortic valve stenosis undergoing transcatheter aortic valve implantation. *Circ Cardiovasc Interv*. 2015;8:e002358. doi: 10.1161/CIRCINTERVENTIONS.114.002358

11. Rosenhek R, Baumgartner H. Aortic sclerosis, aortic stenosis and lipid-lowering therapy. *Expert Rev Cardiovasc Ther*. 2008;6:385–390. doi: 10.1586/14779072.6.3.385

12. Larsson SC, Wolk A, Håkansson N, Bäck M. Overall and abdominal obesity and incident aortic valve stenosis: two prospective cohort studies. *Eur Heart J*. 2017;38:2192–2197. doi: 10.1093/eurheartj/ehx140

13. Martinsson A, Li X, Andersson C, Nilsson J, Smith JG, Sundquist K. Temporal trends in the incidence and prognosis of aortic stenosis: a nationwide study of the Swedish population. *Circulation*. 2015;131:988–994. doi: 10.1161/CIRCULATIONAHA.114.012906

14. Iung B, Vahanian A. Valvular heart diseases in elderly people. *Lancet*. 2006;368:969–971. doi: 10.1016/S0140-6736(06)69216-7

15. Weiss RM, Ohashi M, Miller JD, Young SG, Heistad DD. Calcific aortic valve stenosis in old hypercholesterolemic mice. *Circulation*. 2006;114:2065–2069. doi: 10.1161/CIRCULATIONAHA.106.634139

16. Chu YI, Lund DD, Doshi H, Keen HL, Knudtson KL, Funk ND, Shao JQ, Cheng J, Hajj GP, Zimmerman KA, et al. Fibrotic aortic valve stenosis in hypercholesterolemic/hypertensive mice. *Arterioscler Thromb Vasc Biol*. 2016;36:466–474. doi: 10.1161/ATVBAHA.115.306912

17. Honda S, Miyamoto T, Watanabe T, Narumi T, Kadowaki S, Honda Y, Otaki Y, Hasegawa H, Netsu S, Funayama A, et al. A novel mouse model of aortic valve stenosis induced by direct wire injury. *Arterioscler Thromb Vasc Biol*. 2014;34:270–278. doi: 10.1161/ATVBAHA.113.302610

18. Miller JD, Weiss RM, Heistad DD. Calcific aortic valve stenosis: methods, models, and mechanisms. *Circ Res*. 2011;108:1392–1412. doi: 10.1161/CIRCRESAHA.110.234138

19. Hutcheson JD, Aikawa E, Merryman WD. Potential drug targets for calcific aortic valve disease. *Nat Rev Cardiol*. 2014;11:218–231. doi: 10.1038/nrcardio.2014.1

20. Kluge R, Scherneck S, Schürmann A, Joost H-G. Pathophysiology and genetics of obesity and diabetes in the New Zealand obese mouse: a model of the human metabolic syndrome [Internet]. In: Joost H-G, Al-Hasani H, Schürmann A, eds. *Animal Models in Diabetes Research*. Humana Press; 2012:59–73. Available at: https://link.springer.com/protocol/10.1007/978-1-62703-068-7_5. Accessed August 9, 2019. doi: 10.1007/978-1-62703-068-7_5

21. Ortlepp JR, Kluge R, Giesen K, Plum L, Radke P, Hanrath P, Joost HG. A metabolic syndrome of hypertension, hyperinsulinaemia and hypercholesterolaemia in the New Zealand obese mouse. *Eur J Clin Invest*. 2000;30:195–202. doi: 10.1046/j.1365-2362.2000.00611.x

22. Grune J, Blumrich A, Brix S, Jeuthe S, Drescher C, Grune T, Foryst-Ludwig A, Messroghli D, Kuebler WM, Ott C, et al. Evaluation of a commercial multi-dimensional echocardiography technique for ventricular volumetry in small animals. *Cardiovasc Ultrasound*. 2018;16:10. doi: 10.1186/s12947-018-0128-9

23. Grune J, Benz V, Brix S, Salatzki J, Blumrich A, Höft B, Klopfleisch R, Foryst-Ludwig A, Kolkhof P, Kintscher U. Steroidal and nonsteroidal mineralocorticoid receptor antagonists cause differential cardiac gene expression in pressure overload-induced cardiac hypertrophy. *J Cardiovasc Pharmacol*. 2016;67:402–411. doi: 10.1097/FJC.0000000000000366

24. Douglas PS, Morrow R, Ioli A, Reichek N. Left ventricular shape, afterload and survival in idiopathic dilated cardiomyopathy. *J Am Coll Cardiol*. 1989;13:311–315. doi: 10.1016/0735-1097(89)90504-4

25. Markwald RR, Norris RA, Moreno-Rodriguez R, Levine RA. Developmental basis of adult cardiovascular diseases: valvular heart diseases. *Ann N Y Acad Sci*. 2010;1188:177–183. doi: 10.1111/j.1749-6632.2009.05098.x

26. Conway SJ, Doetschman T, Azhar M. The inter-relationship of periostin, TGF beta, and BMP in heart valve development and valvular heart diseases. *ScientificWorldJournal*. 2011;11:1509–1524. doi: 10.1100/tsw.2011.132

27. Lincoln J, Kist R, Scherer G, Yutzey KE. Sox9 is required for precursor cell expansion and extracellular matrix organization during mouse heart valve development. *Dev Biol*. 2007;305:120–132. doi: 10.1016/j.ydbio.2007.02.002

28. Bi W, Deng JM, Zhang Z, Behringer RR, de Crombrugghe B. Sox9 is required for cartilage formation. *Nat Genet*. 1999;22:85–89. doi: 10.1038/8792

29. Stein PD, Sabbah HN, Pitha JV. Continuing disease process of calcific aortic stenosis: role of microthrombi and turbulent flow. *Am J Cardiol*. 1977;39:159–163. doi: 10.1016/S0002-9149(77)80185-9

30. Baumgartner H, Hung J, Bermejo J, Chambers JB, Evangelista A, Griffin BP, Iung B, Otto CM, Pellikka PA, Quiñones M; American Society of Echocardiography, European Association of Echocardiography. Echocardiographic assessment of valve stenosis: EAE/ASE recommendations for clinical practice. *J Am Soc Echocardiogr*. 2009;22:1–23; quiz 101–102. doi: 10.1016/j.echo.2008.11.029

31. Maeder MT, Weber L, Buser M, Gerhard M, Haager PK, Maisano F, Rickli H. Pulmonary hypertension in aortic and mitral valve disease. *Front Cardiovasc Med*. 2018;5:40. Available at: https://www.frontiersin.org/articles/10.3389/fcvm.2018.00040/full. Accessed July 14, 2019. doi: 10.3389/fcvm.2018.00040

32. Thenappan T, Gomberg-Maitland M. Epidemiology of pulmonary hypertension and right ventricular failure in left heart failure. *Curr Heart Fail Rep*. 2014;11:428–435. doi: 10.1007/s11897-014-0216-6

33. Grune J, Beyhoff N, Hegemann N, Lauryn JH, Kuebler WM. From bedside to bench: lung ultrasound for the assessment of pulmonary edema in animal models. *Cell Tissue Res*. 2020;380:379–392. doi: 10.1007/s00441-020-03172-2

34. Rosenkranz S, Lang IM, Blindt R, Bonderman D, Bruch L, Diller GP, Felgendreher R, Gerges C, Hohenforst-Schmidt W, Holt S, et al. Pulmonary hypertension associated with left heart disease: updated recommendations of the Cologne Consensus Conference 2018. *Int J Cardiol*. 2018;272S:53–62. doi: 10.1016/j.ijcard.2018.08.080

35. Mahmut A, Boulanger M-C, El Husseini D, Fournier D, Bouchareb R, Després J-P, Pibarot P, Bossé Y, Mathieu P. Elevated expression of lipoprotein-associated phospholipase A2 in calcific aortic valve disease: implications for valve mineralization. *J Am Coll Cardiol*. 2014;63:460–469. doi: 10.1016/j.jacc.2013.05.105

36. O'Brien KD, Reichenbach DD, Marcovina SM, Kuusisto J, Alpers CE, Otto CM. Apolipoproteins B, (a), and E accumulate in the morphologically early lesion of "degenerative" valvular aortic stenosis. *Arterioscler Thromb Vasc Biol*. 1996;16:523–532. doi: 10.1161/01.ATV.16.4.523

37. Thanassoulis G, Campbell CY, Owens DS, Smith JG, Smith AV, Peloso GM, Kerr KF, Pechlivanis S, Budoff MJ, Harris TB, et al. Genetic associations with valvular calcification and aortic stenosis. *N Engl J Med*. 2013;368:503–512. doi: 10.1056/NEJMoa1109034

38. Bonow RO, Greenland P. Population-wide trends in aortic stenosis incidence and outcomes. *Circulation*. 2015;131:969–971. doi: 10.1161/CIRCULATIONAHA.115.014846

39. Rosenhek R, Klaar U, Schemper M, Scholten C, Heger M, Gabriel H, Binder T, Maurer G, Baumgartner H. Mild and moderate aortic stenosis: natural history and risk stratification by echocardiography. *Eur Heart J*. 2004;25:199–205. doi: 10.1016/j.ehj.2003.12.002

40. Otto CM, Burwash IG, Legget ME, Munt BI, Fujioka M, Healy NL, Kraft CD, Miyake-Hull CY, Schwaegler RG. Prospective study of asymptomatic valvular aortic stenosis: clinical, echocardiographic, and exercise predictors of outcome. *Circulation*. 1997;95:2262–2270. doi: 10.1161/01.CIR.95.9.2262

41. Gošev I, Zeljko M, Đurić Ž, Nikolić I, Gošev M, Ivčević S, Bešić D, Legčević Z, Paić F. Epigenome alterations in aortic valve stenosis and its related left ventricular hypertrophy. *Clin Epigenetics*. 2017;9:106. doi: 10.1186/s13148-017-0406-7

42. Coté N, Mahmut A, Bosse Y, Couture C, Pagé S, Trahan S, Boulanger M-C, Fournier D, Pibarot P, Mathieu P. Inflammation is associated with the remodeling of calcific aortic valve disease. *Inflammation*. 2013;36:573–581. doi: 10.1007/s10753-012-9579-6

43. Beydoun HA, Beydoun MA, Liang H, Dore GA, Shaked D, Zonderman AB, Eid SM. Sex, race, and socioeconomic disparities in patients with aortic stenosis (from a Nationwide Inpatient Sample). *Am J Cardiol*. 2016;118:860–865. doi: 10.1016/j.amjcard.2016.06.039

44. Bienjonetti-Boudreau D, Fleury M-A, Voisine M, Paquin A, Chouinard I, Tailleur M, Duval R, Magnan P-O, Beaudoin J, Salaun E, et al. Impact of sex on the management and outcome of aortic stenosis patients. *Eur Heart J*. 2021;42:2683–2691. doi: 10.1093/eurheartj/ehab242

45. John C, Grune J, Ott C, Nowotny K, Deubel S, Kühne A, Schubert C, Kintscher U, Regitz-Zagrosek V, Grune T. Sex differences in cardiac mitochondria in the New Zealand obese mouse. *Front Endocrinol*. 2018;9:732. https://www.frontiersin.org/article/10.3389/fendo.2018.00732/full. Accessed February 28, 2019.

46. Lindman BR, Bonow RO, Otto CM. Current management of calcific aortic stenosis. *Circ Res*. 2013;113:223–237. doi: 10.1161/CIRCRESAHA.111.300084

47. Joseph L, Krishnaswamy A, Tuzcu EM, Sonny A, Ozkan A, Svensson LG, Griffin BP, Thomas J, Kapadia SR. Relation of cuspal asymmetry to development of aortic stenosis in adults with tricuspid aortic valves. *J Heart Valve Dis*. 2014;23:395–405.

48. Pawade TA, Newby DE, Dweck MR. Calcification in aortic stenosis: the skeleton key. *J Am Coll Cardiol*. 2015;66:561–577. doi: 10.1016/j.jacc.2015.05.066

49. Groom DA, Starke WR. Cartilaginous metaplasia in calcific aortic valve disease. *Am J Clin Pathol*. 1990;93:809–812. doi: 10.1093/ajcp/93.6.809

50. Hinton RB, Lincoln J, Deutsch GH, Osinska H, Manning PB, Benson DW, Yutzey KE. Extracellular matrix remodeling and organization in developing and diseased aortic valves. *Circ Res*. 2006;98:1431–1438. doi: 10.1161/01.RES.0000224114.65109.4e

51. Lindman BR, Clavel M-A, Mathieu P, Iung B, Lancellotti P, Otto CM, Pibarot P. Calcific aortic stenosis. *Nat Rev Dis Primers*. 2016;2:16006. doi: 10.1038/nrdp.2016.6

52. Stephens EH, Saltarrelli JG, Baggett LS, Nandi I, Kuo JJ, Davis AR, Olmsted-Davis EA, Reardon MJ, Morrisett JD, Grande-Allen KJ. Differential proteoglycan and hyaluronan distribution in calcified aortic valves. *Cardiovasc Pathol*. 2011;20:334–342. doi: 10.1016/j.carpath.2010.10.002

53. Schlotter F, Halu A, Goto S, Blaser MC, Body SC, Lee LH, Higashi H, DeLaughter DM, Hutcheson JD, Vyas P, et al. Spatiotemporal

multi-omics mapping generates a molecular atlas of the aortic valve and reveals networks driving disease. *Circulation*. 2018;138:377–393. doi: 10.1161/CIRCULATIONAHA.117.032291

54. Artiach G, Carracedo M, Seime T, Plunde O, Laguna-Fernandez A, Matic L, Franco-Cereceda A, Bäck M. Proteoglycan 4 is increased in human calcified aortic valves and enhances valvular interstitial cell calcification. *Cells*. 2020;9:E684. doi: 10.3390/cells9030684

55. Hulin A, Moore V, James JM, Yutzey KE. Loss of Axin2 results in impaired heart valve maturation and subsequent myxomatous valve disease. *Cardiovasc Res*. 2017;113:40–51. doi: 10.1093/cvr/cvw229

56. Fang M, Alfieri CM, Hulin A, Conway SJ, Yutzey KE. Loss of β-catenin promotes chondrogenic differentiation of aortic valve interstitial cells. *Arterioscler Thromb Vasc Biol*. 2014;34:2601–2608. doi: 10.1161/ATVBAHA.114.304579

57. Cheek JD, Wirrig EE, Alfieri CM, James JF, Yutzey KE. Differential activation of valvulogenic, chondrogenic, and osteogenic pathways in mouse models of myxomatous and calcific aortic valve disease. *J Mol Cell Cardiol*. 2012;52:689–700. doi: 10.1016/j.yjmcc.2011.12.013

58. Peacock JD, Levay AK, Gillaspie DB, Tao G, Lincoln J. Reduced Sox9 function promotes heart valve calcification phenotypes in vivo. *Circ Res*. 2010;106:712–719. doi: 10.1161/CIRCRESAHA.109.213702

59. Lincoln J, Lange AW, Yutzey KE. Hearts and bones: shared regulatory mechanisms in heart valve, cartilage, tendon, and bone development. *Dev Biol*. 2006;294:292–302. doi: 10.1016/j.ydbio.2006.03.027

60. Norris RA, Damon B, Mironov V, Kasyanov V, Ramamurthi A, Moreno-Rodriguez R, Trusk T, Potts JD, Goodwin RL, Davis J, et al. Periostin regulates collagen fibrillogenesis and the biomechanical properties of connective tissues. *J Cell Biochem*. 2007;101:695–711. doi: 10.1002/jcb.21224

61. Butcher JT, Norris RA, Hoffman S, Mjaatvedt CH, Markwald RR. Periostin promotes atrioventricular mesenchyme matrix invasion and remodeling mediated by integrin signaling through Rho/PI 3-kinase. *Dev Biol*. 2007;302:256–266. doi: 10.1016/j.ydbio.2006.09.048

62. Hakuno D, Kimura N, Yoshioka M, Mukai M, Kimura T, Okada Y, Yozu R, Shukunami C, Hiraki Y, Kudo A, et al. Periostin advances atherosclerotic and rheumatic cardiac valve degeneration by inducing angiogenesis and MMP production in humans and rodents. *J Clin Invest*. 2010;120:2292–2306. doi: 10.1172/JCI40973

63. Breitling S, Ravindran K, Goldenberg NM, Kuebler WM. The pathophysiology of pulmonary hypertension in left heart disease. *Am J Physiol Lung Cell Mol Physiol*. 2015;309:L924–L941. doi: 10.1152/ajplung.00146.2015

64. Kerem A, Yin J, Kaestle SM, Hoffmann J, Schoene AM, Singh B, Kuppe H, Borst MM, Kuebler WM. Lung endothelial dysfunction in congestive heart failure: role of impaired Ca^{2+} signaling and cytoskeletal reorganization. *Circ Res*. 2010;106:1103–1116. doi: 10.1161/CIRCRESAHA.109.210542

65. Kingsbury MP, Huang W, Donnelly JL, Jackson E, Needham E, Turner MA, Sheridan DJ. Structural remodelling of lungs in chronic heart failure. *Basic Res Cardiol*. 2003;98:295–303. doi: 10.1007/s00395-003-0419-6

66. Meng Q, Lai Y-C, Kelly NJ, Bueno M, Baust JJ, Bachman TN, Goncharov D, Vanderpool RR, Radder JE, Hu J, et al. Development of a mouse model of metabolic syndrome, pulmonary hypertension, and heart failure with preserved ejection fraction. *Am J Respir Cell Mol Biol*. 2017;56:497–505. doi: 10.1165/rcmb.2016-0177OC

67. Robbins IM, Newman JH, Johnson RF, Hemnes AR, Fremont RD, Piana RN, Zhao DX, Byrne DW. Association of the metabolic syndrome with pulmonary venous hypertension. *Chest*. 2009;136:31–36. doi: 10.1378/chest.08-2008

68. Nair A, Jacob S. A simple practice guide for dose conversion between animals and human. *J Basic Clin Pharm*. 2016;7:27. doi: 10.4103/0976-0105.177703

69. Kohut A, Patel N, Singh H. Comprehensive echocardiographic assessment of the right ventricle in murine models. *J Cardiovasc Ultrasound*. 2016;24:229–238. doi: 10.4250/jcu.2016.24.3.229

70. Villalba-Orero M, López-Olañeta MM, González-López E, Padrón-Barthe L, Gómez-Salinero JM, García-Prieto J, Wai T, García-Pavía P, Ibáñez B, Jiménez-Borreguero LJ, et al. Lung ultrasound as a translational approach for non-invasive assessment of heart failure with reduced or preserved ejection fraction in mice. *Cardiovasc Res*. 2017;113:1113–1123. doi: 10.1093/cvr/cvx090

Supplemental Material

Data S1.

Supplemental Methods and Results

Echocardiography

Echocardiography of both ventricles, the aorta, and the lung was performed using a Vevo® 3100 high-resolution Imaging System coupled to a MX400 ultra-high frequency linear array transducer (18-38 MHz, center transmit: 30 MHz, axial resolution: 50 µm) (both FUJIFILM VisualSonics, Toronto, Ontario, Canada) as described previously[22,23]. Briefly, mice were exposed to 3% isoflurane (Baxter International, Deerfield, USA) and fixed in a dorsal position on a heating pad to maintain physiological body temperatures. During echocardiographic examination, mice were continuously monitored by ECG recording. The anterior thorax was depilated to optimize the acoustic interface. Pre-warmed ultrasound gel (Parker Laboratories Fairfield, New Jersey, USA) was applied on the chest for echocardiographic image acquisition of B- and M-Mode images of both ventricles and the aorta. Velocity profiles of the aorta, the pulmonary valve outflow (parasternal short axis view at the level of the AoV), and the tricuspid valve (four-chamber view) were assessed using color and pulse wave (PW) Doppler echocardiography. Lung ultrasound (LUS) was performed over the right-side pulmonary field identified by the clearly visible pleural line and pleural space in a parasternal long axis view.

Assessment of AoVs and three-dimensional (3D) echocardiography of the aortic arch were performed using the MX700 ultra-high frequency linear array transducer (30-70 MHz, center transmit: 50 MHz, axial resolution: 30 µm; FUJIFILM VisualSonics). 3D image acquisition was realized with a specialized 3D-motor (FUJIFILM VisualSonics), allowing for automated stepwise movement of the probe, as described by us previously[22]. To this end, a B-mode image obtained at the maximum dimension of the aortic arch served as starting point for consecutive image recordings (3D range: 3.5–4 mm (depending on the size of the aortic arch), frequency: 50 MHz, step size: 50 µm). AoVs were recorded in a parasternal short axis view at the level of the AoV using ECG-gated kilohertz visualization (EKV, 1000 Hz), allowing increased temporo-spatial

resolution by averaging multiple cardiac cycles. All acquired images were digitally stored in raw format (DICOM) for further offline analyses.

Echocardiographic Image Analyses

Image analyses were performed by a trained expert in small animal echocardiography using the dedicated software package VevoLAB Version 3.1.0 (FUJIFILM VisualSonics) LV dimensions, RV dimensions and RV function were calculated from acquired M-Mode images in a parasternal long axis view. A minimum of two independent M-Mode images and 3 consecutive cardiac cycles, respectively, was analyzed, resulting in n>6 subsequently averaged values per individual animal. Global LV systolic function and heart rate were assessed from two independent B-Mode images derived from parasternal long axis views. Calculation of LV function was based on endocardial border tracing from LV outflow tract to apex using the monoplane Simpson's method of discs. For calculation of cardiac index, we extrapolated body surface area from body weights by a species-specific formula for mice[68] and matched it to cardiac output values assessed on the same day in the same animal. Doppler signals were analyzed over a minimum of five cardiac cycles per individual animal and measurements were subsequently averaged. In line with the clinical scenario, we classified AS severity by using the ascending aortic peak velocity profiles of B6 and NZO mice[30]. AS grades were defined as followed: no AS≤2500mm/s (no hemodynamic relevant AS), AS I=2500-3000mm/s (mild), AS II=3000-4000mm/s (moderate) and AS III≥4000mm/s (severe). Pulmonary artery measurements and calculation of the RV index of myocardial performance (RIMP) were carried out as described previously[69]. Stored LUS cine loops were scored according to the mouse lung ultrasound score (MoLUS), considering lung sliding during respiration, predominant line profile, echography color and pleural abnormalities[70]. 3D cine loops of the aorta were loaded into the 4D-analyses tool of VevoLab. The maximum dimension of the aortic arch was identified by browsing through the cubical view of the cine loop. The contour of the aortic arch was traced by starting 0.3 mm inward of the brachiocephalic artery. A total of 40 contours with a step size of 0.1 mm (yielding a total tracing distance of 4 mm) were drawn. To evaluate a completed tracing, the 3D reconstruction was reviewed by a second observer to exclude tracing irregularities.

IHC staining (H&E, PS)

All slides underwent deparaffinization and subsequent rehydration via a decreasing ethanol series. For H&E staining, slides were placed in Haemalaun solution (Carl Roth, Karlsruhe, Germany) for 3 min, followed by tap water washing for 10 min and 30 s of dH_2O. Next, 1% aqueous eosin solution (Eosin Y, Fluka 45240) was added for 1 min followed by another washing step. Picrosirius (PS) red staining was carried out using Sirius Red solution (0.5g Direct red 80 (365548, Sigma-Aldrich) in 500 ml saturated picric acid (Morphisto 10339) for 1 h at RT. Afterwards, slides were washed twice in 0.5 % acetic acid for only few seconds and excess dye was washed out. After H&E and PS staining, slides were dehydrated and mounted with Histofluid (6900002, Engelbrecht, Germany).

Histology- IHC staining AoVs (H&E, PS, Alizarin Red, Movat's stain)

Whole hearts of BL6 mice in the 22nd week of age and of NZO mice in the 12th (n=3) and 22nd (n=4) week of age were harvested for histopathological investigation of AoVs in short axis view. Samples were fixed for 24 h in 4 % Formalin (Thermo Scientific, Waltham, USA) and then stored in 70% ethanol. After microdissection of aortic roots, tissue samples were embedded in Tissue-Tek OCT compound (Sakura Finetek, Alphen aan den Rijn, The Netherlands), frozen in 2-methylbutane (Thermo Scientific) cooled with dry ice and sectioned into 6-µm slices. Special care was taken that aortic valves were kept intact to ensure best quality of the histological analyses. Samples were stained with H&E (mentioned above) to visualize the anatomic and morphologic structure of aortic valves. Longitudinal cross-sections of AoVs from BL6 and NZO mice were used for PS (see above), Alizarin Red and Movat's stain.

For Alizarin Red staining, paraformaldehyde-fixed AoVs were deparaffinized and rehydrated to dH_2O. Slides were stained with Alizarin Red Solution (2 g Alizarin Red S (K844, Fluka, Germany)) solved in 100 ml dH_2O, pH adjusted to 4.1~4.3 using 10 % ammonium hydroxide) for 2.5 min. Excess dye was washed out and samples dehydrated in acetone (20 s) followed by Acetone-Xylene (1:1) solution (20 s). Finally, samples were cleared in xylene and mounted with Histofluid.

For Movat`s stain deparaffinized and rehydrated slides were placed 10 min in 1% aqueous Alcian Blue solution (Alcian blue 8GS Chroma 1A288) followed by 5 min of tap water washing and 1 h incubation in alkaline ethanol (Morphisto 10132). Afterwards

slides were washed 10 min in tap water and 1 min in dH$_2$O. Following, slides were placed 10 min in Weigerts Hematoxylin (Chroma A: 2E032 + B: 2E052, Waldeck GmbH&Co.KG, Germany) before washed once more with tap water for 15 min. Next, Brilliant Crocein-Acid Fuchsine (Chroma1B109/Chroma1B525 4:1, Waldeck GmbH&Co.KG, Germany) was added for 15 min followed by washing the slides with 0.5 % acetic acid. Afterwards, slides were placed 20 min in 5 % Phosphotungstic acid (Chroma 3D092, Waldeck GmbH&Co.KG, Germany) followed by washing with 0.5 % acetic acid. Next, slides were washed with 100% ethanol 3 times for 5 min, followed by 1h incubation with Saffron du Gatinais (Chroma 5A394, Waldeck GmbH&Co.KG, Germany). Afterwards slides were washed with 100% ethanol 3 times for 5 min and finalized by two times for 5 min toluene and permanently embedding of the sections with Histofluid (yellow: collagen; blue-green: proteoglycans cartilage/tissue, dark-red: osteoid, red: elastic fibers; black: nuclei, reddish: cytoplasm; light blue: acid glucosaminoglycan).

Immunofluorescence staining AoVs (periostin and Sox9))

For immunofluorescence analysis of periostin and Sox9, sections were deparaffinized and rehydrated in Roti-Histol (Carl Roth, Karlsruhe, Germany) followed by a decreasing ethanol series. For heat-mediated antigen retrieval, slides were placed in citrate-buffer (10mM cirtrate acid, 0.05% Tween 20 in dH$_2$O) for 20 min at 95°C in a water bath, followed by cooling over 15 min at RT and blocking (Antibody Diluent, Agilent, Waldbronn, Germany), containing 10 % goat serum for 1 h. Rabbit anti-periostin (ab215499, abcam, Berlin, Germany, 1:500) and rabbit anti-Sox9 (#82630T, cell signaling, Frankfurt, Germany, 1:100) diluted in blocking solution were used as primary antibodies and incubated for 1 h in a lightproof humidified chamber at RT. Afterwards, slides were incubated with AlexaFluor 488 secondary antibody for 30 min (Invitrogen, Darmstadt, Germany) and mounted with FluorCare mounting medium containing DAPI (Carl Roth, Karlsruhe, Germany).

Histology- IHC antibody staining: CD68 and α-SMA

For CD68 and α-SMA, slides we deparaffinized, rehydrated and heat-mediated antigen retrieval and blocking was performed as above. Additionally, sections were blocked with 0.03 % hydrogen peroxide (Peroxidase block; Agilent) for 10 min at RT, followed by incubation with primary antibodies for 1 h in a lightproof humidified chamber at RT. Rabbit anti-CD68 antibody (ab125212, Abcam, Cambridge, UK) was used, followed by

a 30-min incubation with horseradish peroxidase-labeled polymer. Next, tissue sections were incubated with substrate-chromogen solution, 3,3′-Diaminobenzidin (EnVision+ system-HRP (DAB), Agilent Waldbronn, Germany), counterstained with hematoxylin (Sigma-Aldrich, Taufkirchen, Germany) and mounted with Entellan (Merck Millipore, Darmstadt, Germany). For anti-alpha smooth muscle actin (α-SMA) staining, lung sections were incubated with rabbit anti-α-SMA antibody (ab5694, Abcam, Germany) at 4°C overnight, followed by a 30 min incubation with the secondary antibody (414341F, rabbit anti-Histofine, Medac, Wedel, Germany) at RT (detection via HRP/DAB system as described above).

Histological analyses

For overview images, longitudinal and cross-sectional heart slides and lungs were scanned using a MIRAX scanner (Zeiss, Ulm, Germany), which allows to obtain digitized images of whole stained organ sections (scale 2000 µm, 200 µm). Histological staining's of hearts and lungs were scanned and analyzed with AxioCamMRm (Zeiss, Oberkochen, Germany) and CaseViewer Software Version 2.3 (3DHISTECH Ltd, Budapest, Hungary).

Quantitative analyses

α-SMA lung staining

α-SMA lung staining was analyzed in at least 50 microvessels per animal by grading the muscularization status as non-, partially or fully muscularized. Medial wall thickness was determined in H&E staining by measuring the external and internal diameter of all detectable 20-50 µm vessels and 50-150 µm vessels per cross section (average vessel number analyzed per mouse: 20-50 µm vessels = 13.9; 50-150 mm vessels = 9.8). Relative vessel wall thickness was calculated as (external diameter–internal diameter)/(external diameterx100). Absolute vessel wall thickness in µm was calculated as (external diameter-internal diameter)/2.

Mean area/size of heart/valve tissue

Quantification of mean heart/valve tissue area was performed using the image analysis tool of the Zeiss Zen 3.0 (blue edition) software, obtaining the area in pixel². For heart cross section we analyzed and compared the total area in pixel² and for valve size

quantification we calculated the mean area of all valve leaflets per sample that could be detected.

PS red-stained collagen content in heart/lung sections

Quantification of PS red-stained collagen content in lung sections was performed using the image analysis tool of the Zeiss ZEN 3.0 (blue edition) software, calculating the percentage fraction of PS red-stained collagen fibers (total stained pixel²) relative to the total heart/lung area (yellow, total pixel²).

Penetrance of aortic valve thickening phenotype

Semi-quantitative analysis of aortic valve thickening was performed by a blinded expert in veterinary pathology. H&E-stained aortic valves of age-matched, male B6 and male/female NZO mice were graded to assess the degree of valve thickening as follows: 0=none, 1=mild, 2=moderate, 3=severe thickening of aortic valve leaflets, respectively.

Triglyceride measurements

Plasma triglyceride (TG) levels of BL6 and NZO mice in the 22nd week of age were measured by a colorimetric assay according to the manufacturer's instructions (A11A01640, HORIBA Europe GmbH, Oberursel, Germany) using the ABX Pentra 400 benchtop analyzer (Horiba, Kyoto, Japan).

Figure S1 Metabolic Phenotype of NZO-mice.
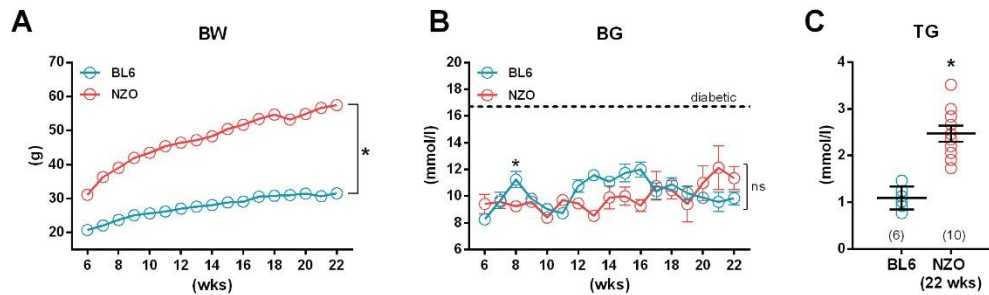
A Weekly monitored body weight (BW) of BL6 and NZO mice (BL6: r=0.967, 95%CI=0.910 to 0.989, p<0.0001; NZO: r=0.968, 95%CI=0.914 to 0.989, p<0.0001). **B** Blood glucose (BG) levels of BL6 and NZO mice (BL6: r=0.242, 95%CI=-0.270 to 0.648, p=0.349; NZO: r=0.705, 95%CI=0.339 to 0.886, p=0.002). Dashed line was set as landmark and indicates a BG level of 16.6 mmol/l, which was considered as manifest diabetes. Repeated measures ANOVA (A and B) **C** Triglyceride (TG) content measured in serum samples of BL6 and NZO mice. Data are represented as mean±SEM. *p<.05 vs. age-matched BL6 controls. n-numbers are indicated in brackets.

Figure S2. Side-by-side comparison of the histological aortic valve phenotype in male and female NZO mice.
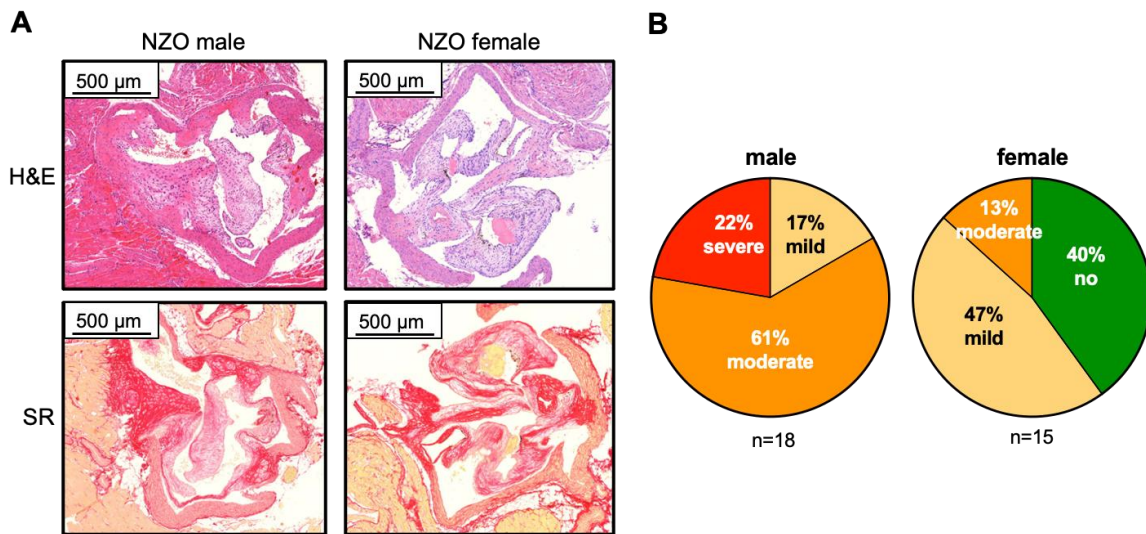

A Exemplary images of H&E and Picrosirius Red (SR) stained aortic valves from male and female NZO mice (both 22 weeks). **B** Semi-quantitative analyses of aortic valve thickening and abnormal valve morphology of H&E-stained aortic valves from male (n=18) and female (n=15) NZO mice. 0=none, 1=mild, 2=moderate and 3=severe thickening of aortic valve leaflets, respectively.

Figure S3. Alizarin red staining of aortic valves in NZO mice.

unstained | Alizarin Red
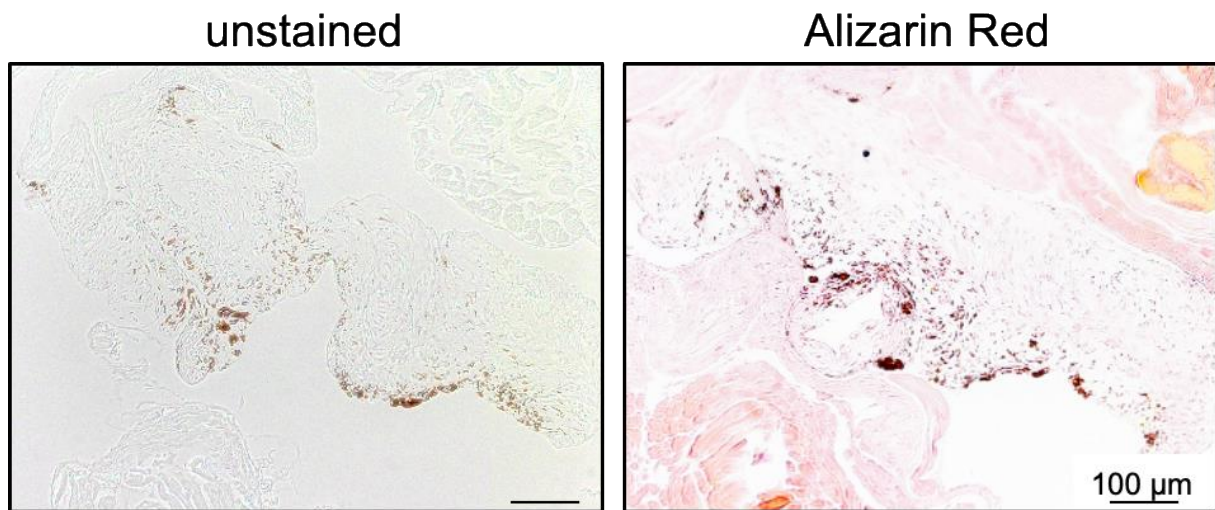
The exemplary images show mild calcific aortic valve disease in a male NZO mouse at the age of 34 weeks (right). Parts of the positive signal in Alizarin Red staining might be caused by melanocytes, as indicated by including a unstained control section from the same animal (left).

Figure S4. RV/LV dynamics.
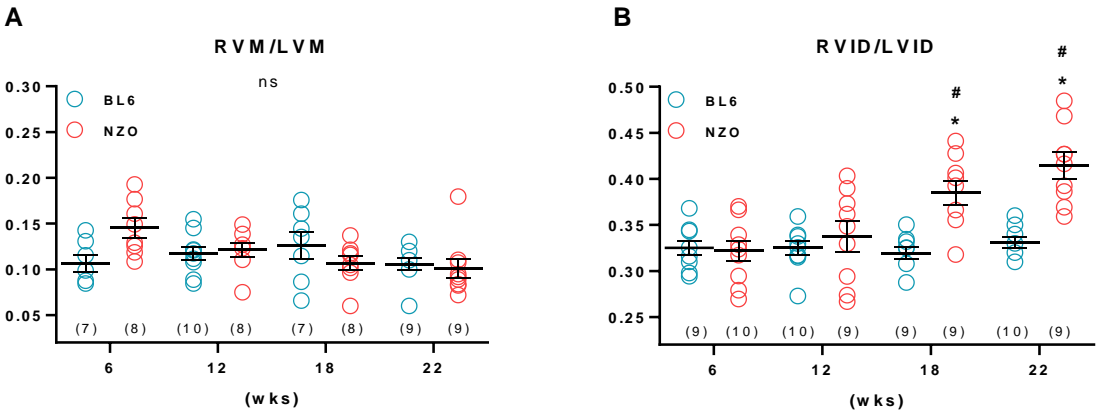
A Right ventricular (RV) internal diameter-to-left ventricular (LV) internal diameter-ratio (RVID/LVID) and **B** RV mass-to-LV mass-ratio (RVM/LVM) as assessed via echocardiography. Data are represented as mean±SEM *p<.05 vs. age matched BL6 controls, #p<.05 vs. baseline measurement at 6th week of age, n-numbers are indicated in brackets.

Supplemental Video Legends:

Video S1. Exemplary 3D reconstruction of aortic arch of BL6 control mouse.

Best viewed with Windows Media Player.

Video S2. Exemplary 3D reconstruction of aortic arch of NZO mouse. Best

viewed with Windows Media Player.

Video S3. Exemplary lung ultrasound cine loop of BL6 control mouse. Best

viewed with Windows Media Player.

Video S4. Exemplary lung ultrasound cine loop of NZO mouse. Best viewed with

Windows Media Player.